A consistent discrete element method for quasi-static and dynamic elasto-plasticity

Frédéric Marazzato, Alexandre Ern, Laurent Monasse

A consistent discrete element method for quasi-static and dynamic elasto-plasticity

Frédéric Marazzato[1,2,3], Alexandre Ern[1,3] and Laurent Monasse[1,4]
[1]Université Paris-Est, Cermics (ENPC), F-77455 Marne-la-Vallée cedex 2, France
email: {alexandre.ern, frederic.marazzato}@enpc.fr
[2]CEA, DAM, DIF, F-91297 Arpajon, France
[3]Inria Paris, EPC SERENA, F-75589 Paris, France
[4] Université Côte d'Azur, Inria, CNRS, LJAD, EPC COFFEE, 06108 Nice, France
email: laurent.monasse@inria.fr

November 1, 2019

Abstract

We propose a new discrete element method supporting general polyhedral meshes. The method can be understood as a lowest-order discontinuous Galerkin method parametrized by the continuous mechanical parameters (Young's modulus and Poisson's ratio). We consider quasi-static and dynamic elasto-plasticity, and in the latter situation, a pseudo-energy conserving time-integration method is employed. The computational cost of the time-stepping method is moderate since it is explicit and used with a naturally diagonal mass matrix. Numerical examples are presented to illustrate the robustness and versatility of the method for quasi-static and dynamic elasto-plastic evolutions.

1 Introduction

Discrete element methods (DEM) constitute a large class of particle methods which have originally been used for crystalline materials [15] and geotechnical problems [8] and have found applications in granular materials, soil and rock mechanics. In their original formulation, DEM consisted in representing a domain by small spherical particles interacting by means of forces and torques. A wide range of models for the expression of these bonds has been developed depending on the material constitutive law. Computing the deformation of the domain then consists in computing the evolution of the particle system. Advantages of DEM are their ability to deal with discontinuous materials, such as fractured or porous materials, as well as the possibility to take advantage of GPU computations [23]. Other, similar, particle methods have been derived in the context of Smooth Particles Hydrodynamics (SPH) methods, which require an interaction kernel [13]. The main difficulty in DEM consists in deriving a correct set of forces between elements to discretize the continuous equations (in the present case, dynamic elasto-plasticity). DEM originally used sphere packing to discretize the domain [17] and were forced to fit parameters in order to obtain relevant values for the Young modulus E or the Poisson ratio ν [16, 6]. Moreover simulating a material with a Poisson ratio ν larger than 0.3 met with difficulties [2]. Note also the possibility to use DEM only in a limited zone, where crack occurs for instance, in order to mitigate these issues. For example, a modified DEM (MDEM) has been coupled with a consistent virtual element method (VEM) for elasticity to discretize fracturing porous media [20].

A discrete element method was developed in [19] and was formally proved to be consistent with Cauchy elasticity. A first attractive feature of this method was that the discrete force

parameters were directly derived from the Young modulus and the Poisson ratio without the need for a fitting process. Moreover the method exhibited robustness in the incompressibility limit ($\nu \to 0.5$). Similar ideas have been used to handle brittle fracture [1]. However several limitations remain in this approach. First the evaluation of the forces between particles hinges on the use of a Voronoi mesh and does not adapt to general (not even tetrahedral) meshes. This is due to a nearest-neighbour evaluation of the gradient on a facet of the mesh (known in the Finite Volume community as the "two-point flux problem"). Secondly the expression of the forces for a Cauchy continuum cannot be readily extended to more general behaviour laws. Finally the convergence proof is mostly formal (on a Cartesian grid) and no convergence proof is given on general (Voronoi) meshes, apart from numerical evidence.

The main goal of the present contribution is to circumvent the above issues by extending the discrete element method of [19] to general polyhedral meshes and elasto-plastic behaviour laws. The present particle method can be viewed as a space-discretization scheme with a diagonal mass matrix, and as such shares a number of properties with finite volumes [11, 12] and lowest-order discontinuous Galerkin (dG) methods [9]. Specifically we use piecewise constant gradient reconstructions in each mesh cell evaluated from local displacement reconstructions at the facets of the mesh. Volumetric unknowns are also added to compute plastic strains. We devise the scheme for both quasi-static and dynamic elasto-plasticity, and in the latter situation we perform the time discretization using the explicit pseudo-energy conserving time-integration method developed in [18]. Numerical results are presented to illustrate the robustness and versatility of the proposed method in two and three space dimensions. Finally the convergence of the scheme can be studied using the framework of gradient discretization methods (GDM) [10]. GDM lead to a unified and powerful framework allowing one to prove convergence and error estimates for a wide range of numerical schemes.

This paper is organised as follows. Section 2 briefly recalls the equations of dynamic elasto-plasticity in a Cauchy continuum. Section 3 introduces the proposed DEM and presents the space discretization of the governing equations. Some numerical tests to verify the convergence of the space discretization in a steady setting are reported. Section 4 deals with the DEM discretization for quasi-static elasto-plasticity and presents test cases in two and three space dimensions. Section 5 addresses the time discretization of the dynamic elasto-plasticity problem using the explicit pseudo-energy conserving time-integrator developed in [18]. This section also assesses the coupled DEM and time discretization on test cases in three space dimensions. Finally Section 6 draws some conclusions.

2 Governing equations for dynamic elasto-plasticity

We consider an elasto-plastic material occupying the domain $\Omega \subset \mathbb{R}^d$, $d \in \{2, 3\}$, in the reference configuration and evolving dynamically on the finite time interval $(0, T)$, $T > 0$, under the action of volumetric forces and boundary conditions. The strain regime is restricted to small strains so that the linearized strain tensor is $\varepsilon(u) := \frac{1}{2}(\nabla u + (\nabla u)^{\mathsf{T}})$, where u is the displacement field. The plastic constitutive law hinges on a von Mises criterion with nonlinear isotropic hardening. The material is supposed to be homogeneous, isotropic and rate-independent. The presented formalism can be extended to the case of anisotropic, inhomogeneous, rate-dependent, anisothermal materials as well as finite strains. The stress tensor σ is such that

$$\sigma := \mathbb{C} : (\varepsilon(u) - \varepsilon_p), \tag{1}$$

where $\mathbb{C}$ is the fourth-order stiffness tensor and ε_p is the (trace-free) tensor of remanent plastic strain. The von Mises yield function φ is given by

$$\varphi(\sigma, p) := \sqrt{\frac{3}{2}}|\mathrm{dev}(\sigma)| - (\sigma_0 + R(p)), \tag{2}$$

where $\mathrm{dev}(\sigma)$ is the deviatoric part of σ and $|\tau| = (\sum_{i,j=1}^d \tau_{ij}^2)^{\frac{1}{2}}$ for a second-order tensor τ, p is the scalar cumulated plastic deformation, $R(p) := \frac{d\omega_p}{dp}$ where the function ω_p is the part of the Helmholtz free energy related to isotropic hardening, and σ_0 is the initial yield stress, so that the actual yield stress is $\sigma_0 + R(p)$. Admissible states are characterized by the inequality $\varphi(\sigma, p) \le 0$, the material is in the elastic domain if $\varphi(\sigma, p) < 0$ and in the plastic domain if $\varphi(\sigma, p) = 0$.

In strong form, the dynamic elasto-plasticity equations consist in searching for the displacement field $u : (0,T) \times \Omega \to \mathbb{R}^d$, the remanent plastic strain tensor $\varepsilon_p : (0,T) \times \Omega \to \mathbb{R}^{d\times d}$, and the scalar cumulated plastic deformation $p : (0,T) \times \Omega \to \mathbb{R}$ such that the following equations hold in Ω for all $t \in (0,T)$:

$$\begin{cases} \rho\ddot{u} - \mathrm{div}(\sigma) = f, \\ \varphi(\sigma, p) \le 0, \\ \lambda = \dot{p} \ge 0, \quad \lambda\varphi(\sigma, p) = 0, \quad \dot{\varepsilon}_p = \lambda \dfrac{\partial \varphi}{\partial \sigma}(\sigma), \end{cases} \tag{3}$$

where $\rho > 0$ is the density of the material, dots indicate time derivatives, f is the imposed volumetric force, and λ is the Lagrange multiplier associated with the constraint $\varphi(\sigma, p) \le 0$. Note that owing to (2), we have $\dot{\varepsilon}_p = \lambda\sqrt{\frac{3}{2}}\frac{\mathrm{dev}(\sigma)}{|\mathrm{dev}(\sigma)|}$, so that $\dot{p} = \lambda = \sqrt{\frac{2}{3}}|\dot{\varepsilon}_p|$.

Let $\partial\Omega = \partial\Omega_N \cup \partial\Omega_D$ be a partition of the boundary of Ω. By convention $\partial\Omega_D$ is a closed set and $\partial\Omega_N$ is a relatively open set in $\partial\Omega$. The boundary $\partial\Omega_D$ has an imposed displacement u_D, whereas a normal stress g is imposed on $\partial\Omega_N$, i.e. we enforce

$$u = u_D \ \text{ on } (0,T) \times \partial\Omega_D, \qquad \sigma \cdot n = g_N \ \text{ on } (0,T) \times \partial\Omega_N. \tag{4}$$

Note that u_D and g_N can be time-dependent. Finally the initial conditions prescribe that $u(0) = u_0$, $\dot{u}(0) = v_0$ and $p(0) = 0$ in Ω.

To formulate the governing equations (3) together with the Neumann boundary condition (4) in weak form, we consider time-dependent functions with values in space-dependent functional spaces. Let us set

$$V_D := \left\{ v \in H^1(\Omega; \mathbb{R}^d) \mid v_{|\partial\Omega_D} = u_D \right\}, \qquad V_0 := \left\{ v \in H^1(\Omega; \mathbb{R}^d) \mid v_{|\partial\Omega_D} = 0 \right\}. \tag{5}$$

(Note that the space V_D is actually time-dependent if the Dirichlet data is time-dependent.) We also set

$$Q := L^2(\Omega; \mathbb{R}^{d\times d}), \qquad Q_0 := \{\eta_p \in Q \mid \mathrm{tr}(\eta_p) = 0\}, \tag{6}$$

and $P := L^2(\Omega)$. Here $L^2(\Omega; \mathbb{R}^q)$, $q \ge 1$, is the Hilbert space composed of $\mathbb{R}^q$-valued square-integrable functions in Ω, and $H^1(\Omega; \mathbb{R}^q)$ is the subspace of $L^2(\Omega; \mathbb{R}^q)$ composed of those functions whose weak gradient is also square-integrable. All of the above functional spaces are equipped with their natural inner product. Then the weak solution is searched as a triple $(u, \varepsilon_p, p) : (0,T) \to V_D \times Q_0 \times P$. To alleviate the mathematical formalism, we do not specify here the regularity in time (see [14] and [5]). We introduce the mass bilinear form such that

$$m(a, \tilde{v}) := \langle \rho a, \tilde{v} \rangle_{V_0', V_0}, \quad \forall (a, \tilde{v}) \in V_0' \times V_0, \tag{7}$$

where V_0' denotes the dual space of V_0 and $\langle\cdot,\cdot\rangle_{V_0',V_0}$ the duality pairing, and the stiffness bilinear form parameterized by a member $\eta_p \in Q_0$ such that

$$a(\eta_p; v, \tilde{v}) := \int_\Omega (\mathbb{C} : (\varepsilon(v) - \eta_p)) : \varepsilon(\tilde{v}), \quad \forall (v, \tilde{v}) \in V_D \times V_0, \tag{8}$$

The governing equations (3) are rewritten as follows: Find $(u, \varepsilon_p, p) : (0,T) \to V_D \times Q_0 \times P$ such that, for all $t \in (0,T)$,

$$\begin{cases} m(\ddot{u}(t), \tilde{v}) + a(\varepsilon_p(t); u(t), \tilde{v}) = l(t; \tilde{v}), & \forall \tilde{v} \in V_0, \\ \varphi(\sigma, p) \le 0, & \text{in } \Omega, \\ \lambda = \dot{p} \ge 0, \quad \lambda\varphi(\sigma, p) = 0, \quad \dot{\varepsilon}_p = \lambda \dfrac{\partial \varphi}{\partial \sigma}(\sigma), & \text{in } \Omega. \end{cases} \tag{9}$$

where the time-dependency is left implicit in the second and third equations, and with the linear form $l(t)$ acting on V_0 as follows:

$$l(t; \tilde{v}) := \int_\Omega f(t) \cdot \tilde{v} + \int_{\partial\Omega_N} g_N(t) \cdot \tilde{v}. \tag{10}$$

Note that the Dirichlet condition is enforced strongly, whereas the Neumann condition is enforced weakly. Define the elastic energy $E_{\text{elas}}(t) := \frac{1}{2}\int_\Omega \sigma(t) : \mathbb{C}^{-1} : \sigma(t)$ with $\sigma(t) := \mathbb{C} : (\varepsilon(u(t)) - \varepsilon_p(t))$, $E_{\text{kin}}(t) := \frac{1}{2} m(\dot{u}(t), \dot{u}(t))$, $E_{\text{plas}}(t) := \int_\Omega \sigma_0 p(t) + \omega_p(p(t))$, and $E_{\text{ext}}(t) := \int_0^T l(t; \dot{u}(t))$. Then assuming for simplicity a homogeneous Dirichlet condition, we have the following energy balance equation:

$$E_{\text{elas}}(t) + E_{\text{kin}}(t) + E_{\text{plas}}(t) = E_{\text{ext}}(t). \tag{11}$$

3 Space semi-discretization

In this section we present the DEM space semi-discretization of the weak formulation (9), and we present a few verification test cases for static linear elasticity.

3.1 Degrees of freedom

The domain Ω is discretized with a mesh $\mathcal{T}_h$ of size h made of polyhedra with planar facets in three space dimensions or polygons with straight edges in two space dimensions. We assume that Ω is itself a polyhedron or a polygon so that the mesh covers Ω exactly and we also assume that the mesh is compatible with the partition of the boundary $\partial\Omega$ into the Dirichlet and Neumann parts.

Let $\mathcal{C}$ denote the set of mesh cells and $\mathcal{Z}^\partial$ the set of mesh vertices sitting on the boundary of Ω. Vector-valued volumetric degrees of freedom (dofs) for a generic displacement field $v_\mathcal{C} := (v_c)_{c\in\mathcal{C}} \in \mathbb{R}^{d\#(\mathcal{C})}$ are placed at the barycentre of every mesh cell $c \in \mathcal{C}$, where $\#(S)$ denotes the cardinality of a set S. Additional vector-valued boundary degrees of freedom $v_{\mathcal{Z}^\partial} := (v_z)_{z\in\mathcal{Z}^\partial} \in \mathbb{R}^{d\#(\mathcal{Z}^\partial)}$ for the displacement are added at every boundary vertex $z \in \mathcal{Z}^\partial$. The reason why we introduce boundary vertex dofs is motivated in Section 3.3. These dofs are also used to enforce the Dirichlet condition on $\partial\Omega_D$. We use the compact notation $v_h := (v_\mathcal{C}, v_{\mathcal{Z}^\partial})$ for the collection of all the cell dofs and all the boundary vertex dofs. Figure 1 illustrates the position of the displacement dofs. In addition a (trace-free) tensor-valued dof representing the internal plasticity variable $\eta_{p,c} \in \mathbb{R}^{d\times d}$ is attached to every mesh cell $c \in \mathcal{C}$, as well as a scalar dof p_c representing the cumulated plastic deformation. We write $\eta_{p,\mathcal{C}} := (\eta_{p,c})_{c\in\mathcal{C}} \in Q_h := \mathbb{R}^{(d^2-1)\#(\mathcal{C})}$ and $p_\mathcal{C} := (p_c)_{c\in\mathcal{C}} \in P_h := \mathbb{R}^{\#(\mathcal{C})}$.

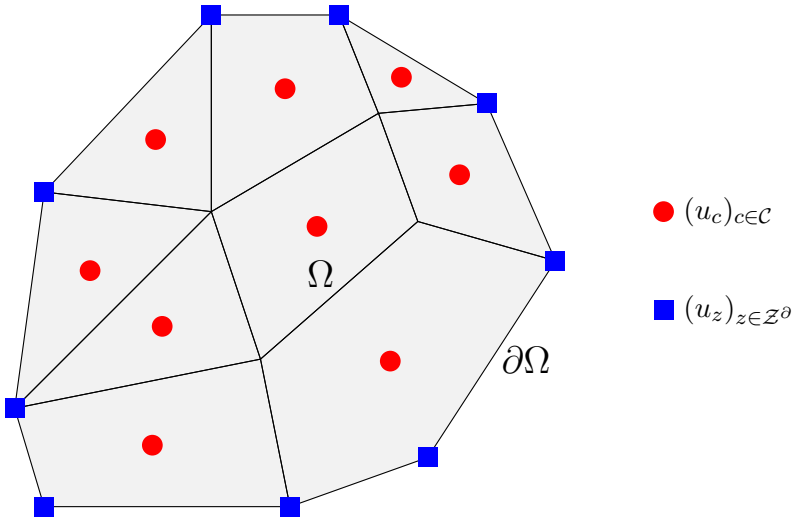

Figure 1: Continuum Ω covered by a polyhedral mesh and vector-valued degrees of freedom for the displacement.

Let $\mathcal{F}$ denote the set of mesh facets. We partition this set as $\mathcal{F} = \mathcal{F}^i \cup \mathcal{F}^b$, where $\mathcal{F}^i$ is the collection of the internal facets shared by two mesh cells and $\mathcal{F}^b$ is the collection of the boundary facets sitting on the boundary $\partial\Omega$ (such facets belong to the boundary of only one mesh cell). Using the cell and boundary-vertex dofs introduced above, we reconstruct a collection of displacements $v_\mathcal{F} := (v_F)_{F\in\mathcal{F}} \in \mathbb{R}^{d\#(\mathcal{F})}$ on the mesh facets. The facet reconstruction operator is denoted $\mathcal{R}$ and we write

$$v_\mathcal{F} := \mathcal{R}(v_h). \tag{12}$$

The precise definition of the facet reconstruction operator is given in Section 3.3. Using the reconstructed facet displacements, it is possible using a discrete Stokes formula to devise a discrete $\mathbb{R}^{d\times d}$-valued piecewise-constant gradient field for the displacement that we write $G_\mathcal{C}(v_\mathcal{F}) := (G_c(v_\mathcal{F}))_{c\in\mathcal{C}} \in \mathbb{R}^{d^2\#(\mathcal{C})}$. Specifically we set in every mesh cell $c \in \mathcal{C}$,

$$G_c(v_\mathcal{F}) := \sum_{F\in\partial c} \frac{|F|}{|c|} v_F \otimes n_{F,c}, \qquad \forall v_\mathcal{F} \in \mathbb{R}^{d\#(\mathcal{F})}, \tag{13}$$

where the summation is over the facets F of c and $n_{F,c}$ is the outward normal to c on F. Note that for all $v_h \in V_h$, we have

$$G_c(\mathcal{R}(v_h)) = \sum_{F\in\partial c} \frac{|F|}{|c|} (\mathcal{R}(v_h)_F - v_c) \otimes n_{F,c}, \tag{14}$$

since $\sum_{F\in\partial c} |F| n_{F,c} = 0$. Finally we define a constant linearized strain tensor in every mesh cell $c \in \mathcal{C}$ such that

$$\varepsilon_c(v_\mathcal{F}) := \frac{1}{2}(G_c(v_\mathcal{F}) + G_c(v_\mathcal{F})^\mathsf{T}) \in \mathbb{R}^{d\times d}. \tag{15}$$

3.2 Discrete problem

Let us set $V_h := \mathbb{R}^{d\#(\mathcal{C})} \times \mathbb{R}^{d\#(\mathcal{Z}^\partial)}$ and (recall that $\partial\Omega_D$ is a closed set)

$$\begin{cases} V_{hD} := \{v_h \in V_h \mid v_z = u_D(z)\ \forall z \in \mathcal{Z}^\partial \cap \partial\Omega_D\}, \\ V_{h0} := \{v_h \in V_h \mid v_z = 0\ \forall z \in \mathcal{Z}^\partial \cap \partial\Omega_D\}. \end{cases} \tag{16}$$

(Note that the space V_{hD} is actually time-dependent if the Dirichlet data is time-dependent.) The discrete stiffness bilinear form is parameterized by a member $\eta_{p,\mathcal{C}} \in Q_h$ and is such that, for all $(v_h, \tilde{v}_h) \in V_{hD} \times V_{h0}$ (compare with (8)),

$$a_h(\eta_{p,\mathcal{C}}; v_h, \tilde{v}_h) := \sum_{c\in\mathcal{C}} |c|(\mathbb{C} : (\varepsilon_c(\mathcal{R}(v_h)) - \eta_{p,c})) : \varepsilon_c(\mathcal{R}(\tilde{v}_h)) + s_h(v_h, \tilde{v}_h). \tag{17}$$

Here s_h is a weakly consistent stabilization bilinear form intended to render a_h coercive and which is defined on $V_h \times V_h$ as follows:

$$s_h(v_h, \tilde{v}_h) = \sum_{F\in\mathcal{F}^i} |F|\frac{\eta}{h_F}[v_\mathcal{C}]_F \cdot [\tilde{v}_\mathcal{C}]_F + \sum_{F\in\mathcal{F}^b} |F|\frac{\eta}{h_F}(\mathcal{R}(v_h)_F - v_{c_-}) \cdot (\mathcal{R}(\tilde{v}_h)_F - \tilde{v}_{c_-}), \tag{18}$$

where h_F is the diameter of the facet $F \in \mathcal{F}$ and where $v_\mathcal{C}$ and $\tilde{v}_\mathcal{C}$ collect the cell dofs of v_h and $\tilde{v}_h$, respectively. For an interior facet $F \in \mathcal{F}^i$, writing c_- and c_+ the two mesh cells sharing F, i.e., $F = \partial c_- \cap \partial c_+$, and orienting F by the unit normal vector n_F pointing from c_- to c_+, one has $[v_\mathcal{C}]_F := v_{c_-} - v_{c_+}$. The sign of the jump is irrelevant in what follows. The role of the summation over the interior facets in (18) is to penalize the jumps of the cell dofs across the interior facets. For a boundary facet $F \in \mathcal{F}^b$, we denote c_- the unique mesh cell containing F and we orient F by the unit normal vector $n_F := n_{c_-}$ which points outward Ω. The role of the summation over the boundary facets in (18) is to penalize the jumps between the cell dofs and the boundary vertex dofs. The parameter $\eta > 0$ in (18) is user-defined with the only requirement that $\eta > 0$. In practice a very small, but positive, value is taken in our simulations, of the order of 10^{-6} times the Young modulus.

We can next define a discrete mass bilinear form m_h similar to (7) and a discrete load linear form $l_h(t)$ similar to (10); details are given below. Then the space semi-discrete version of the evolution problem (9) amounts to seeking $(u_h, \varepsilon_{p,\mathcal{C}}, p_\mathcal{C}) : (0, T) \to V_{hD} \times Q_h \times P_h$ such that, for all $t \in (0, T)$,

$$\begin{cases} m_h(\ddot{u}_h(t), \tilde{v}_h) + a_h(\varepsilon_{p,\mathcal{C}}(t); u_h(t), \tilde{v}_h) = l_h(t, \tilde{v}_h), & \forall \tilde{v}_h \in V_{h0}, \\ \varphi(\Sigma_c(u_h), p_c) \le 0, & \forall c \in \mathcal{C}, \\ \lambda_c = \dot{p}_c \ge 0, \quad \lambda_c\varphi(\Sigma_c(u_h), p_c) = 0, \quad \dot{\varepsilon}_{p,c} = \lambda_c \dfrac{\partial\varphi}{\partial\sigma}(\Sigma_c(u_h)), & \forall c \in \mathcal{C}, \end{cases} \tag{19}$$

where the time-dependency is left implicit in the second and third equations and where we introduced in every mesh cell $c \in \mathcal{C}$ the local stress tensor

$$\Sigma_c(u_h) := \mathbb{C} : (\varepsilon_c(\mathcal{R}(u_h)) - \varepsilon_{p,c}) \in \mathbb{R}^{d\times d}. \tag{20}$$

Note that the plasticity relations in (19) are enforced cellwise, i.e., a mesh cell $c \in \mathcal{C}$ is either in the elastic state or in the plastic state depending on the value of $\varphi(\Sigma_c(u_h), p_c)$.

The definition of the discrete mass bilinear form m_h hinges on subdomains to condense the mass associated with the dofs. Figure 2 represents our choice for the subdomains. For all the interior cells, the subdomain ω_c is chosen as the whole cell, i.e., $\omega_c = c$. For the boundary vertices and for the cells having a boundary face, a dual barycentric subdomain is constructed, leading to subdomains denoted by ω_z and ω_c, respectively (see Figure 2). For the discrete load linear form, we compute averages of the external loads f and g_N in the mesh cells and on the Neumann boundary facets, respectively. As a consequence, m_h and $l_h(t)$ can be written as follows for all $(v_h, \tilde{v}_h) \in V_h \times V_h$ (compare with (7) and (10)):

$$m_h(v_h, \tilde{v}_h) := \sum_{z\in\mathcal{Z}^\partial} m_z v_z \cdot \tilde{v}_z + \sum_{c\in\mathcal{C}} m_c v_c \cdot \tilde{v}_c, \tag{21}$$

$$l_h(t, \tilde{w}_h) := \sum_{c\in\mathcal{C}} f_c(t) \cdot \tilde{w}_c + \sum_{F\in\mathcal{F}^b\cap\partial\Omega_N} g_F(t) \cdot \mathcal{R}(\tilde{v}_h)_F, \tag{22}$$

with $m_z := \int_{\omega_z} \rho$, $m_c := \int_{\omega_c} \rho$, $f_c(t) := \int_c f(t)$ and $g_F(t) := \int_F g_N(t)$.

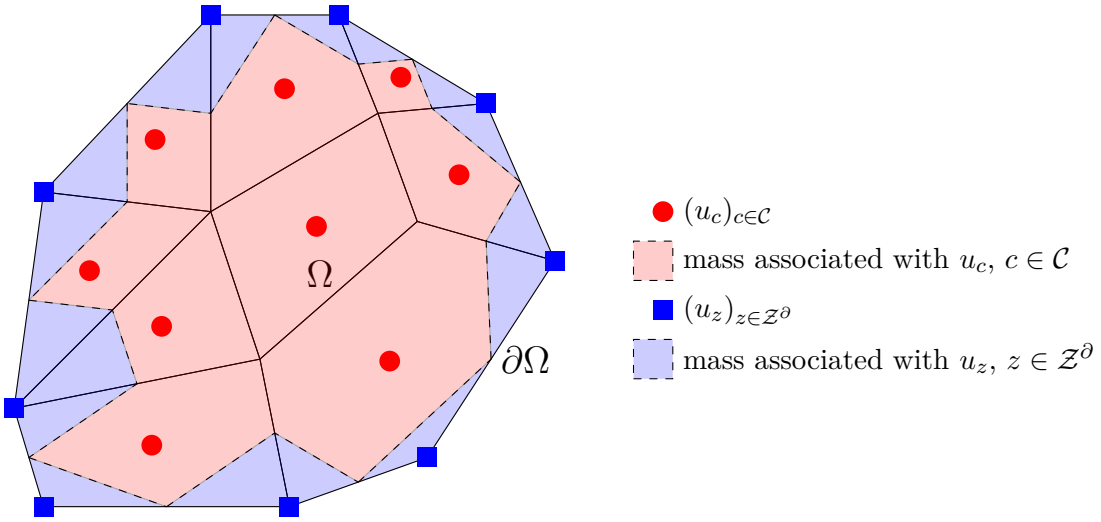

Figure 2: Integration domains to determine the mass associated with the displacement dofs.

3.3 Reconstruction operator on facets

The reconstruction operator $\mathcal{R}$ is constructed in the same way as in the finite volume methods studied in [12, Sec. 2.2] and in the cell-centered Galerkin methods from [9]. For a given facet $F \in \mathcal{F}$, we select neighbouring boundary vertices collected in the subset $\mathcal{Z}_F^\partial$ and neighbouring cells collected in the subset $\mathcal{C}_F$, as well as coefficients $(\alpha_F^z)_{z\in\mathcal{Z}_F^\partial}$ and $(\alpha_F^c)_{c\in\mathcal{C}_F}$, and we set

$$\mathcal{R}(v_h)_F := \sum_{z\in\mathcal{Z}_F^\partial} \alpha_F^z v_z + \sum_{c\in\mathcal{C}_F} \alpha_F^c v_c, \qquad \forall v_h \in V_h. \tag{23}$$

The neighbouring dofs should stay $\mathcal{O}(h)$ close to the facet F. The coefficients α_F^z and α_F^c are chosen as the barycentric coordinates of the facet barycenter x_F in terms of the location of the boundary vertices in $\mathcal{Z}_F^\partial$ and the barycenters of the cells in $\mathcal{C}_F$. Thus they verify

$$\sum_{z\in\mathcal{Z}_F^\partial} \alpha_F^z + \sum_{c\in\mathcal{C}_F} \alpha_F^c = 1, \qquad \forall F \in \mathcal{F}. \tag{24}$$

The main rationale for choosing the neighboring dofs is to ensure as much as possible that all the coefficients α_F^z or α_F^c lie in the interval $(0,1)$, so that the definition of $\mathcal{R}(v_h)_F$ in (23) is based on an interpolation formula (rather than an extrapolation formula if some coefficients lie outside the interval $(0,1)$.) For most internal facets $F \in \mathcal{F}^i$, far from the boundary $\partial\Omega$, it is possible to choose an interpolation-based reconstruction operator using only cell dofs, i.e., we usually have $\mathcal{Z}_F^\partial := \emptyset$. Figure 3 presents an example for an interior facet F using three neighbouring cell dofs located at the cell barycenters x^i, x^j and x^k. Close to the boundary $\partial\Omega$, the use of boundary vertex dofs helps to prevent extrapolation. In all the cases we considered, interpolation was always possible using the algorithm described below.

On the boundary facets, the reconstruction operator only uses interpolation from the boundary vertices of the facet, i.e., we always set $\mathcal{C}_F := \emptyset$ for all $F \in \mathcal{F}^b$. In three space dimensions, the facet can be polygonal and the barycentric coordinates are generalized barycentric coordinates. This is achieved using [4] and the package 2D Triangulation of the geometric library CGAL. In the case of simplicial facets (triangles in three space dimensions and segments in two space dimensions), this procedure reduces to a classical barycentric interpolation.

The advantage of using interpolation rather than extrapolation is relevant in the context of explicit time-marching schemes where the time step is restricted by a CFL condition depending

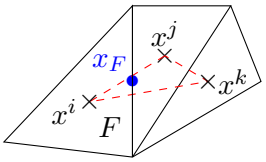

Figure 3: Dofs associated with the interior facet F used for the reconstruction.

on the largest eigenvalue $\lambda_{\max}$ of the stiffness matrix associated with the discrete bilinear form $a_h(0;\cdot,\cdot)$ (see, e.g., (40)). It turns out that using extrapolation can have quite an adverse effect on the maximal eigenvalue of the stiffness matrix, thereby placing quite a severe restriction on the time step, and this restriction is significantly alleviated if enough neighboring dofs are used in (23) to ensure that interpolation is being used. We refer the reader to Table 1 below for an illustration.

Let us now briefly outline the algorithm used for selecting the reconstruction dofs associated with a given mesh facet $F \in \mathcal{F}$. This algorithm has to be viewed more as a proof-of-concept than as an optimized algorithm, and we observe that this algorithm is only used in a pre-processing stage of the computations. Fix an integer $I \geq d+1$; in our computations, we took $I = 10$ if $d = 2$ and $I = 25$ if $d = 3$. Let $F \in \mathcal{F}$.

1. Compute a list of points $(x_i)_{1\leq i\leq I}$ ordered by increasing distance to x_F; each point can be either the barycenter of a mesh cell or a boundary vertex. To this purpose, we use the KDTree structure of the `scipy.spatial` module of Python.

2. Find the smallest index $J \in \{d+1,\ldots,I\}$ such that x_F lies in the convex hull of the set $(x_i)_{1\leq i\leq J}$. If there is no such index J, extrapolation must be used. Otherwise find a subset of $(x_i)_{1\leq i\leq J}$ containing $(d+1)$ points and use the barycentric coordinates of the resulting simplex to evaluate the interpolation coefficients to be used in (23).

To illustrate the performance of the above algorithm in alleviating time step restrictions based on a CFL condition, we report in Table 1 as a function of the integer parameter I from the above algorithm the largest eigenvalue $\lambda_{\max}$ of the stiffness matrix and the percentage of the mesh facets where extrapolation has to be used. The results are obtained on the two three-dimensional meshes considered in Section 5.3.1 together with the DEM discretization for the dynamic elasto-plastic evolution of a beam undergoing torsion. The columns labeled $I = 4$ required in very few cases an additional point because the four closest points turned out to be coplanar.

mesh	$I=4$		$I=6$		$I=9$		$I=12$		$I=15$	
coarse	$2{\cdot}10^{10}$	81%	$1{\cdot}10^{10}$	28%	$2{\cdot}10^{06}$	4%	$1{\cdot}10^{06}$	1.3%	$1{\cdot}10^{06}$	0.4%
fine	$5{\cdot}10^{09}$	74%	$5{\cdot}10^{09}$	28%	$9{\cdot}10^{08}$	4.1%	$4{\cdot}10^{08}$	0.8%	$2{\cdot}10^{05}$	0%

Table 1: Largest eigenvalue of the stiffness matrix and percentage of inner facets with extrapolation for various values of the parameter I on the coarse and fine meshes used in the DEM discretizations reported in Section 5.3.1.

3.4 Interpretation as a Discrete Element Method

In this section we rewrite the first equation in (19) as a particle method by introducing the dofs of the discrete displacement $u_h(t) \in V_{hD}$ attached to the mesh cells and to the boundary vertices

lying on the Neumann boundary, which we write $U_{\rm DEM} := (U_p(t))_{p\in\mathcal{P}}$ with $\mathcal{P} := \mathcal{C} \cup \mathcal{Z}_N^\partial$ and $\mathcal{Z}_N^\partial := \{z \in \mathcal{Z}^\partial \mid z \in \partial\Omega_N\}$. Here $\mathcal{P}$ can be viewed as the indexing set for the set of particles. Recalling the definition of the discrete mass bilinear form, we set $m_p := \int_{\omega_c} \rho$ if $p = c \in \mathcal{C}$ and $m_p := \int_{\omega_z} \rho$ if $p = z \in \mathcal{Z}_N^\partial$. Concerning the external loads, we set $F_{\rm DEM}(t) := (F_p(t))_{p\in\mathcal{P}}$ with $F_p(t) := f_c(t) = \int_c f(t)$ if $z = c$ and $F_p(t) := \sum_{F\in\mathcal{F}_z} \alpha_F^z g_F(t) = \sum_{F\in\mathcal{F}_z} \alpha_F^z \int_F g_N(t)$ if $p = z$, where $\mathcal{F}_z \subset \mathcal{F}^b$ is the collection of the boundary faces to which z belongs and the coefficients α_F^z are those used in (23) for the facet reconstruction. Since the Neumann boundary $\partial\Omega_N$ is relatively open in $\partial\Omega$, all the faces in $\mathcal{F}_z$ belong to $\partial\Omega_N$ if $z \in \mathcal{Z}_N^\partial$.

Recall that $\varepsilon_{p,\mathcal{C}} : (0,T) \to Q_h$ is the discrete tensor of remanent plastic strain. Let us use the shorthand notation $\Sigma_c(t) := \Sigma_c(u_h(t))$ as defined in (20), as well as $\Sigma_\mathcal{C}(t) := (\Sigma_c(t))_{c\in\mathcal{C}}$. For a piecewise-constant function defined on the mesh cells, say $w_\mathcal{C} = (w_c)_{c\in\mathcal{C}}$, we define the mean-value $\{w_\mathcal{C}\}_F := \frac{1}{2}(w_{c_-} + w_{c_+})$ for all $F = \partial c_- \cap \partial c_+ \in \mathcal{F}^i$. Recall that the interior facet F is oriented by the unit normal vector n_F pointing from c_- to c_+ and that the jump across $F \in \mathcal{F}^i$ is defined such that $[w_\mathcal{C}]_F := w_{c_-} - w_{c_+}$. Recall also that for a boundary facet $F \in \mathcal{F}^b$, c_- denotes the mesh cell to which F belongs and that n_F is the unit normal vector to F pointing outward Ω. Then a direct calculation shows that for all $\tilde v_h \in V_{h0}$,

$$
\begin{aligned}
-a_h(\varepsilon_{p,\mathcal{C}}(t); u_h(t), \tilde v_h) = &\sum_{F\in\mathcal{F}^i} |F|(\{\Sigma_\mathcal{C}(t)\}_F\cdot n_F)\cdot[\tilde v_\mathcal{C}]_F\\
&+ \sum_{F\in\mathcal{F}^i} |F|([\Sigma_\mathcal{C}(t)]_F\cdot n_F)\cdot(\{\tilde v_\mathcal{C}\}_F - \mathcal{R}(\tilde v_h)_F)\\
&+ \sum_{F\in\mathcal{F}^b} |F|(\Sigma_{c_-}(t)\cdot n_F)\cdot(\tilde v_{c_-} - \mathcal{R}(\tilde v_h)_F)\\
&- \sum_{F\in\mathcal{F}^i} |F|\frac{\eta}{h_F}[u_\mathcal{C}(t)]_F\cdot[\tilde v_\mathcal{C}]_F\\
&- \sum_{F\in\mathcal{F}^b} |F|\frac{\eta}{h_F}(\mathcal{R}(u_h(t))_F - u_{c_-}(t))\cdot(\mathcal{R}(\tilde v_h)_F - \tilde v_{c_-}).
\end{aligned}
\tag{25}
$$

To simplify some expressions, we are going to neglect the second term on the above right-hand side since this term is of higher-order (it is essentially the product of two jumps). Recall that, by definition, the reconstruction operator $\mathcal{R}$ on a boundary facet $F \in \mathcal{F}^b$ makes use only of the vertex dofs of that facet. Then, letting $(\tilde V_p)_{p\in\mathcal{P}}$ be the collection of the dofs of the discrete test function $\tilde v_h$, we infer that

$$
-a_h(\varepsilon_{p,\mathcal{C}}(t); u_h(t), \tilde v_h) \simeq \sum_{p\in\mathcal{P}} \Phi_p^{\rm ep}(t)\cdot\tilde V_p,
\tag{26}
$$

where $\Phi_p^{\rm ep}(t)$ is the elasto-plastic force acting on the particle $p \in \mathcal{P}$. For all $c \in \mathcal{C}$, we have $\Phi_c^{\rm ep}(t) := \sum_{F\in\mathcal{F}_c^i\cup\mathcal{F}_c^N} \Phi_{c,F}^{\rm ep}(t)$ with $\mathcal{F}_c^i := \{F \in \mathcal{F}^i \mid F \subset \partial c\}$, $\mathcal{F}_c^N := \{F \in \mathcal{F}^b \mid F \subset \partial c \cap \partial\Omega_N\}$, and

$$
\Phi_{c,F}^{\rm ep}(t) := \begin{cases} \iota_{c,F}|F|(\{\Sigma_\mathcal{C}(t)\}_F\cdot n_F - \frac{\eta}{h_F}[u_\mathcal{C}(t)]_F) & \text{if } F \in \mathcal{F}_c^i,\\ |F|(\Sigma_{c_-}(t)\cdot n_F - \frac{\eta}{h_F}(u_{c_-}(t) - \mathcal{R}(u_h(t))_F)) & \text{if } F \in \mathcal{F}_c^N, \end{cases}
\tag{27}
$$

with $\iota_{c,F} := n_c\cdot n_F$, and for all $z \in \mathcal{Z}_N^\partial$, we have

$$
\Phi_z^{\rm ep}(t) := -\sum_{F\in\mathcal{F}_z} \alpha_F^z \Phi_{c_-,F}^{\rm ep}(t),
\tag{28}
$$

with $\Phi_{c_-,F}$ defined in (27). Note that the principle of action and reaction is encoded in the fact that $\iota_{c_-,F} + \iota_{c_+,F} = 0$ for all $F = \partial c_- \cap \partial c_+ \in \mathcal{F}^i$. Finally, putting everything together, we infer that the the first equation in (19) becomes

$$
m_p\ddot U_p(t) \simeq \Phi_p^{\rm ep}(t) + F_p(t), \qquad \forall p \in \mathcal{P}.
\tag{29}
$$

Remark 1 (Matrix formulation)**.** *Let us briefly describe the matrix formulation of the space semi-discrete problem* (19) *in the case of elastodynamics, i.e., without plasticity. For simplicity we focus on the pure Neumann problem. A matrix* $\mathbf{R} \in \mathbb{R}^{d\#(\mathcal{F})\times d\#(\mathcal{P})}$ *corresponding to the reconstruction operator* $\mathcal{R}$ *can be constructed. Its entries are the barycentric coefficients of the dofs used for the reconstruction on the face associated with the given line of* $\mathbf{R}$*. The lines of* $\mathbf{R}$ *associated with boundary facets have, by construction, non-zero entries only for boundary vertices degrees of freedom. The linearized strain matrix* $\mathbf{E} \in \mathbb{R}^{d^2\#(\mathcal{C})\times d\#(\mathcal{F})}$ *is composed of the tensorial coefficients* $\frac{1}{2}\frac{|F|}{|c|}(\otimes n_F + n_F\otimes)$ *on the lines associated with the mesh cell* $c \in \mathcal{C}$ *and the columns associated with the facets* $F \subset \partial c$*. The linear elasticity matrix* $\mathbf{C} \in \mathbb{R}^{d^2\#(\mathcal{C})\times d^2\#(\mathcal{C})}$ *can be written as the block-diagonal matrix where each block corresponds to the double contraction with the fourth-order elastic tensor* $\mathbb{C}$ *and multiplication by* $|c|$*. The jump matrix* $\mathbf{J} \in \mathbb{R}^{d\#(\mathcal{F})\times d\#(\mathcal{P})}$ *is composed of lines such that:* (i) *For an interior facet* $F \in \mathcal{F}^i$*, the line contains exactly one* 1 *and one* -1*, corresponding to the connectivity matrix of the facet* F *with the adjacent cells* c_- *and* c_+*;* (ii) *For a boundary facet* $F \in \mathcal{F}^b$*, the line contains* -1 *for the adjacent cell* c_- *and the corresponding coefficients of* $\mathbf{R}$ *for the boundary vertices. Denoting* $\mathbf{D} \in \mathbb{R}^{d\#(\mathcal{F})\times d\#(\mathcal{F})}$ *the diagonal matrix with entry* $\frac{\eta}{h_F}|F|$ *for the facet* F*, the stabilization matrix* $\mathbf{S}$ *corresponding to the bilinear form* s_h *can be written* $\mathbf{S} := \mathbf{J}^\mathsf{T}\mathbf{D}\mathbf{J} \in \mathbb{R}^{d\#(\mathcal{P})\times d\#(\mathcal{P})}$*. Finally, denoting* $\mathbf{K} := \mathbf{R}^\mathsf{T}\mathbf{E}^\mathsf{T}\mathbf{C}\mathbf{E}\mathbf{R} + \mathbf{S} \in \mathbb{R}^{d\#(\mathcal{P})\times d\#(\mathcal{P})}$ *the stiffness matrix, the space semi-discrete system* (19) *in the case of elastodynamics reduces to* $\mathbf{M}\ddot{U}_{\mathrm{DEM}}(t) + \mathbf{K}U_{\mathrm{DEM}}(t) = F_{\mathrm{DEM}}(t)$*.*

3.5 Convergence tests for linear elasticity

The goal of this section is to briefly verify the correct implementation of the method in the case of static linear elasticity by comparing the numerical predictions using DEM with some analytical solutions and reporting the orders of convergence on sequences of uniformly refined meshes. The model problem thus consists of finding $u \in V_D$ such that

$$\int_\Omega \varepsilon(\nabla u) : \mathbb{C} : \varepsilon(\nabla \tilde{u}) = \int_\Omega f \cdot \tilde{u}, \qquad \forall \tilde{u} \in V_0. \tag{30}$$

The energy error $\|u - u_h\|_{\mathrm{en}}$ is based on the reconstructed linearized strain of the discrete solution in each mesh cell, whereas the L^2-error $\|u - \mathfrak{u}_h\|_{L^2(\Omega)}$ is evaluated by means of the piecewise-affine displacement reconstruction $\mathfrak{u}_h$ such that $\mathfrak{u}_{h|c}(x) := u_c + G_c(\mathcal{R}(u_h)) \cdot (x - x_c)$ for all $x \in c$ and all $c \in \mathcal{C}$, where x_c denotes the barycenter of c.

Let us first consider an isotropic two-dimensional elasticity test case in the domain $\Omega = (0,1)^2$ with the Young modulus set to $E = 70 \cdot 10^3$Pa and the Poisson ratio to $\nu = 0.3$. The reference solution is $u(x,y) = \frac{a}{2}(x^2+y^2)(e_x+e_y)$ with $a = 0.8$ and (e_x, e_y) are the Cartesian basis of $\mathbb{R}^2$. The load term f, which is computed accordingly, is $f(x,y) = -a(\lambda+3\mu)(e_x+e_y)$. A non-homogeneous Dirichlet boundary condition is enforced on the whole boundary. Convergence results are reported in Table 2 showing that the energy error converges to first-order with the mesh size and the L^2-error to second-order.

h	dofs	$\|u - \mathfrak{u}_h\|_{L^2(\Omega)}$	order	$\|u - u_h\|_{\mathrm{en}}$	rder
0.03555	4 464	1.13e-4	-	1.86e-2	-
0.01855	17 190	2.82e-5	2.24	9.08e-3	1.06
0.00971	68 502	7.11e-6	1.96	4.61e-3	1.02
0.00495	271 112	1.78e-6	2.04	2.29e-3	1.02

Table 2: Linear elasticity test case: size of the mesh, number of dofs, L^2-error and order of convergence, energy error and order of convergence.

For the second test case, we consider an orthotropic plate with a hole under tensile stress. The domain is a square plate of size $L = 1$ with a hole in its center of radius $R = 0.1$. We only consider one quarter of the domain owing to the symmetries. The material is supposed to be orthotropic homogeneous with Young's moduli $E_x = 100\text{Pa}$, $E_y = 10\text{Pa}$, Poisson ratio $\nu_{xy} = 0.3$, and shear modulus $G_{xy} = 5\text{Pa}$. Figure 4 shows the problem setup together with the boundary conditions. The applied boundary tension on the top boundary is $g = \sigma_\infty n$ with $\sigma_\infty = 0.001\text{N.m}^{-2}$. The left and bottom boundaries are mixed boundaries, where the normal component of the displacement is set to zero as well as the tangential component of the normal stress. This test case is drawn from [3].

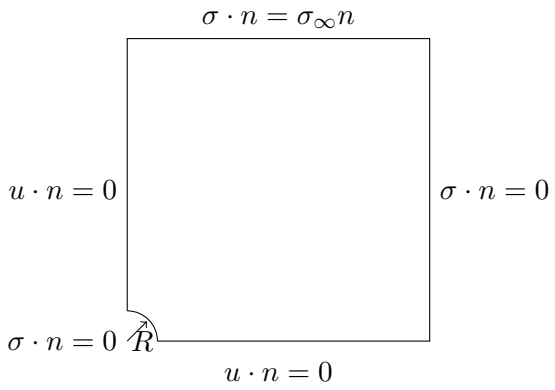

Figure 4: Linear anisotropic elasticity test case: problem setup.

Table 3 reports the energy error and the L^2-error and the orders of convergence. The reference solution is computed on the finest mesh using conforming P^2-Lagrange finite elements (FEM). The convergence rates are slightly lower than in the previous test case, possibly because of the lack of smoothness of the exact solution.

h	dofs	$\|u - u_h\|_{L^2(\Omega)}$	order	$\|u - u_h\|_{\text{en}}$	order
0.21657	276	1.04e-6	-	2.37e-5	-
0.14125	572	5.41e-7	1.80	1.71e-5	0.89
0.06868	2 256	1.69e-7	1.73	9.24e-6	0.90
0.03698	8 764	6.39e-8	1.61	5.60e-6	0.83
0.01807	34 224	3.15e-8	1.45	3.38e-6	0.81
0.00920	147 664	6.27e-9	1.63	1.57e-6	0.86

Table 3: Linear anisotropic elasticity test case: size of the mesh, number of dofs, L^2-error and order of convergence, energy error and order of convergence.

4 Quasi-static elasto-plasticity

In this section we present the quasi-static elasto-plasticity problem, its DEM discretization, and we perform numerical tests to assess the methodology.

4.1 Governing equations

The quasi-static elasto-plastic problem is a simplified formulation of (9) where the intertia term in the mass bilinear form is negligible and where the time derivatives are substituted by discrete

increments. Thus we consider a sequence of loads $l^n \in V_0'$ for all $n = 1, \dots, N$, and we consider the following sequence of problems where $(u^n, \varepsilon_p^n, p^n) \in V_D \times Q_0 \times P$ for all $n = 1, \dots, N$:

$$\begin{cases} a(\varepsilon_p^n; u^n, \tilde{v}) = l^n(\tilde{v}), & \forall \tilde{v} \in V_0, \\ (\varepsilon_p^n, p^n, \mathbb{C}_{\text{ep}}^n, \sigma^n) = \texttt{PLAS\_IMP}(\varepsilon_p^{n-1}, p^{n-1}, \varepsilon^{n-1}, \varepsilon^n), & \text{in } \Omega, \end{cases} \tag{31}$$

where $\varepsilon^{n-1} := \varepsilon(u^{n-1})$, $\varepsilon^n := \varepsilon(u^n)$, and where variables with a superscript $^{n-1}$ come from the solution of the quasi-static problem (31) at the previous load increment or from a prescribed initial condition if $n = 1$. Given a quadruple $(\varepsilon_p^{\text{old}}, p^{\text{old}}, \varepsilon^{\text{old}}, \varepsilon^{\text{new}})$, the procedure `PLAS_IMP` returns a quadruple $(\varepsilon_p^{\text{new}}, p^{\text{new}}, \mathbb{C}_{\text{ep}}^{\text{new}}, \sigma^{\text{new}})$ such that

$$\begin{cases} \varphi(\sigma^{\text{new}}, p^{\text{new}}) \leq 0, \\ \lambda^{\text{new}} := \delta p := p^{\text{new}} - p^{\text{old}} \geq 0, \quad \lambda^{\text{new}} \varphi(\sigma^{\text{new}}, p^{\text{new}}) = 0, \\ \delta\varepsilon_p := \varepsilon_p^{\text{new}} - \varepsilon_p^{\text{old}} = \lambda^{\text{new}} \dfrac{\partial \varphi}{\partial \sigma}(\sigma^{\text{new}}). \end{cases} \tag{32}$$

Moreover $\sigma^{\text{new}} = \mathbb{C} : (\varepsilon^{\text{new}} - \varepsilon_p^{\text{new}})$ is the new stress tensor, and $\mathbb{C}_{\text{ep}}^{\text{new}}$ is the consistent elasto-plastic modulus [21] such that

$$\sigma^{\text{new}} = \sigma^{\text{old}} + \mathbb{C}_{\text{ep}}^{\text{new}} : \delta\varepsilon, \quad \delta\varepsilon := \varepsilon^{\text{new}} - \varepsilon^{\text{old}}, \quad \sigma^{\text{old}} := \mathbb{C} : (\varepsilon^{\text{old}} - \varepsilon_p^{\text{old}}). \tag{33}$$

The consistent elastoplastic modulus is instrumental to solve (31) iteratively using an implicit radial return mapping technique (close to Newton–Raphson iterations) [22]: For all $k \geq 0$, we solve the linear problem in $u^{n,k} \in V_D$ such that

$$\begin{cases} (\mathbb{C}_{\text{ep}}^{n,k} : \varepsilon(u^{n,k+1}), \varepsilon(\tilde{v}))_Q = r^{n,k}(\tilde{v}) := l^n(\tilde{v}) - (\sigma^{n,k}, \varepsilon(\tilde{v}))_Q, & \forall \tilde{v} \in V_0, \\ (\varepsilon_p^{n,k}, p^{n,k}, \mathbb{C}_{\text{ep}}^{n,k}, \sigma^{n,k}) = \texttt{PLAS\_IMP}(\varepsilon_p^{n-1}, p^{n-1}, \varepsilon^{n-1}, \varepsilon^{n,k}), & \text{in } \Omega, \end{cases} \tag{34}$$

where the state for $k = 0$ comes from the previous loading step or the initial condition. Convergence of the iterative process in k is reached when the norm of the residual $r^{n,k}$ is small enough.

4.2 DEM space discretization

Using the DEM space discretization, the sequence of quasi-static problems (31) amounts to seeking a discrete triple $(u_h^n, \varepsilon_{p,\mathcal{C}}^n, p_{\mathcal{C}}^n) \in V_{hD} \times Q_h \times P_h$ for all $n = 1, \dots, N$, such that

$$\begin{cases} a_h(\varepsilon_{p,\mathcal{C}}^n; u_h^n, \tilde{v}_h) = l_h^n(\tilde{v}_h), & \forall \tilde{v}_h \in V_{h0}, \\ (\varepsilon_{p,c}^n, p_c^n, \mathbb{C}_{ep,c}^n, \sigma_c^n) = \texttt{PLAS\_IMP}(\varepsilon_{p,c}^{n-1}, p_c^{n-1}, \varepsilon_{p,c}^{n-1}, \varepsilon_c^n), & \forall c \in \mathcal{C}, \end{cases} \tag{35}$$

where l_h^n represents a suitable discretization of the load linear form l^n. Using the radial return mapping technique as in (34), we solve for all $k \geq 0$ the linear problem in $u_h^{n,k} \in V_{hD}$ such that

$$\begin{cases} \displaystyle\sum_{c \in \mathcal{C}} |c| (\mathbb{C}_{ep,c}^{n,k} : \varepsilon_c(\mathcal{R}(u_h^{n,k+1}))) : \varepsilon_c(\mathcal{R}(\tilde{v}_h)) = r_{\mathcal{C}}^{n,k}(\tilde{v}_h), & \forall \tilde{v}_h \in V_{h0}, \\ (\varepsilon_{p,c}^{n,k}, p_c^{n,k}, \mathbb{C}_{ep,c}^{n,k}, \sigma_c^{n,k}) = \texttt{PLAS\_IMP}(\varepsilon_{p,c}^{n-1}, p_c^{n-1}, \varepsilon_c^{n-1}, \varepsilon_c^{n,k}), & \forall c \in \mathcal{C}, \end{cases} \tag{36}$$

with the residual $r_{\mathcal{C}}^{n,k}(\tilde{v}_h) := l^n(\tilde{v}_h) - \sum_{c \in \mathcal{C}} |c| \sigma_c^{n,k} \cdot \varepsilon_c(\mathcal{R}(\tilde{v}_h))$, and where the discrete state for $k = 0$ comes from the previous loading step or by interpolating the values of the initial condition at the cell barycenters and the boundary vertices. Convergence of the iterative process in k is reached when the norm of the residual $r_{\mathcal{C}}^{n,k}$ is small enough (we use a scaled Euclidean norm).

4.3 Numerical tests

This section contains two three-dimensional tests, a beam in quasi-static flexion and a beam in quasi-static torsion, and a two-dimensional test case on the swelling of an infinite cylinder with internal pressure.

4.3.1 Beam in quasi-static traction

A beam of square section $S = 0.016\text{m}^2$ and $L = 1\text{m}$ is stretched by a displacement $u_D(t)$ imposed at its right extremity, whereas the normal displacement and the tangential component of the normal stress are null at the left extremity. An homogeneous Neumann condition ($\sigma \cdot n = 0$) is enforced on the four remaining sides of the beam. Figure 5 shows a sketch of the problem setup. The Young modulus is taken as $E = 70\text{MPa}$ and the Poisson ratio as $\nu = 0.3$. The yield stress is $\sigma_0 = 250\text{Pa}$, and the material is supposed to be elasto-plastic with linear kinematic hardening. Specifically the tangent plastic modulus is set to $E_t = \frac{1}{10}E$, so that we have $R(p) = Hp$ with $H = \frac{EE_t}{E-E_t}$. The imposed displacement is linearly increased in 20 loading steps from 0 to $3\delta_y$, where $\delta_y = \frac{\sigma_0}{E}L$ is the yield displacement. For this test case the analytical solution is available.

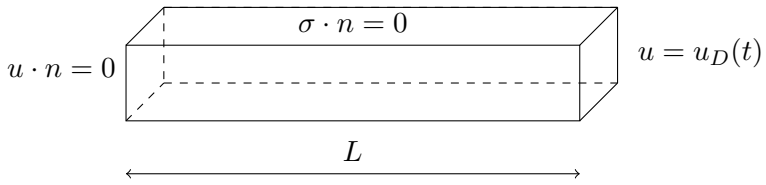

Figure 5: Beam in quasi-static traction: problem setup.

Table 4 reports the energy error and the L^2-error together with the convergence results. These quantities are evaluated as described in Section 3.5. Figure 6 shows the stress-strain response curve, showing perfect agreement with the analytical solution as the mesh is progressively refined. Note that in this test case, the stress tensor is constant in the beam for its only non-zero component (up to symmetry).

h	dofs	$\|u - \mathfrak{u}_h\|_{L^2(\Omega)}$	order	$\|u - u_h\|_{\text{en}}$	order
0.338	894	1.04e-6	-	2.37e-5	-
0.281	1881	5.41e-7	1.80	1.71e-5	0.89
0.236	3483	1.69e-7	1.73	9.24e-6	0.90
0.185	8643	3.15e-8	1.45	3.38e-6	0.81
0.153	17019	6.39e-8	1.61	5.60e-6	0.83

Table 4: Beam in quasi-static traction: size of the mesh, number of dofs, L^2-error and estimated order of convergence, error in energy norm and estimated order of convergence.

4.3.2 Beam in quasi-static torsion

A beam of length $L = 0.2\text{m}$ with a circular section of radius $R = 0.05\text{m}$ is subjected to torsion at one of its extremities. The Young modulus is taken as $E = 70\text{MPa}$ and the Poisson ratio as $\nu = 0.3$. The yield stress is $\sigma_0 = 250\text{Pa}$, and the material is supposed to be perfectly plastic so that $R(p) = 0$. The beam is clamped at one of its extremities, a torsion angle $\alpha(t)$ is imposed at

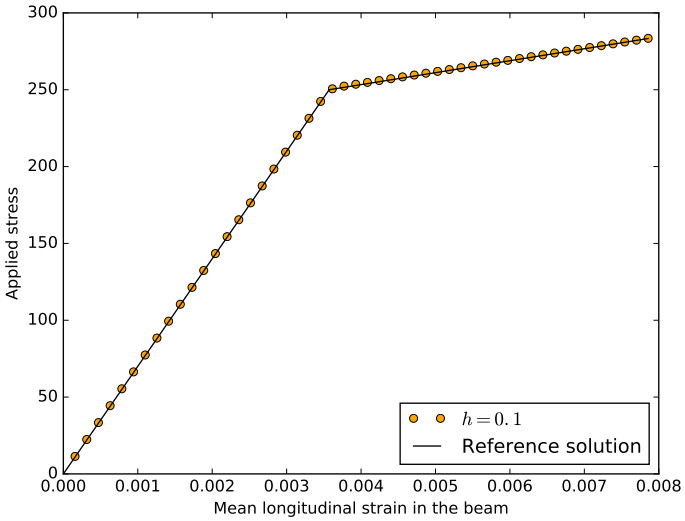

Figure 6: Beam in quasi-static traction: stress-strain response curve for the analytical solution and the DEM solution.

the other extremity, and the rest of the boundary of the beam is stress free ($\sigma \cdot n = 0$). Figure 7 presents the problem setup. The torsion angle $\alpha(t)$ is increased linearly in 20 loading steps from 0 to $\alpha_{\max} = 2\alpha_y$, where $\alpha_y = \frac{\sigma_0 L}{\mu R\sqrt{3}}$ is the yield angle and μ is the second Lamé coefficient. The analytical solution is given in the cylindrical frame (e_r, e_θ, e_z) as $u(r, z, t) = \alpha(t) r \frac{z}{L} e_\theta$.

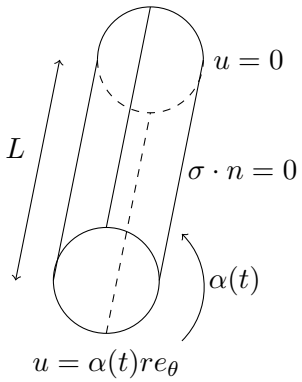

Figure 7: Beam in quasi-static torsion: problem setup.

Table 5 reports the L^2-error on the displacement (evaluated as in Section 3.5) and on the cumulated plastic strain. A reference solution is computed on a fine mesh of size $h = 0.014175$ with P^1-Lagrange FEM. The errors are evaluated as described in Section 3.5. Figure 8 presents the torque-angle response curve for the reference solution and the DEM solution on various meshes, showing good agreement and the convergence of the DEM predictions as the mesh is refined.

4.3.3 Inner swelling of an infinite cylinder

This test case consists in the inner swelling of an infinite cylinder. The inner radius is $R_i = 1$m and the outer radius is $R_o = 1.3$m. Owing to the symmetries, the computation is carried out

h	dofs	$\|u - \mathfrak{u}_h\|_{L^2(\Omega)}$	order	$\|p - p_h\|_{L^2(\Omega)}$	order
0.745	723	7.11e-06	-	1.21e-04	-
0.05881	3021	9.69e-07	4.18	8.06e-05	0.85
0.03294	12726	5.78e-07	2.63	5.81e-05	0.77
0.02871	18996	4.56e-07	2.52	4.95e-05	0.82
0.01965	47670	2.46e-07	2.41	4.04e-05	0.79

Table 5: Beam in quasi-static torsion: size of the mesh, number of dofs, L^2-error in u and order of convergence, L^2-error in p and order of convergence.

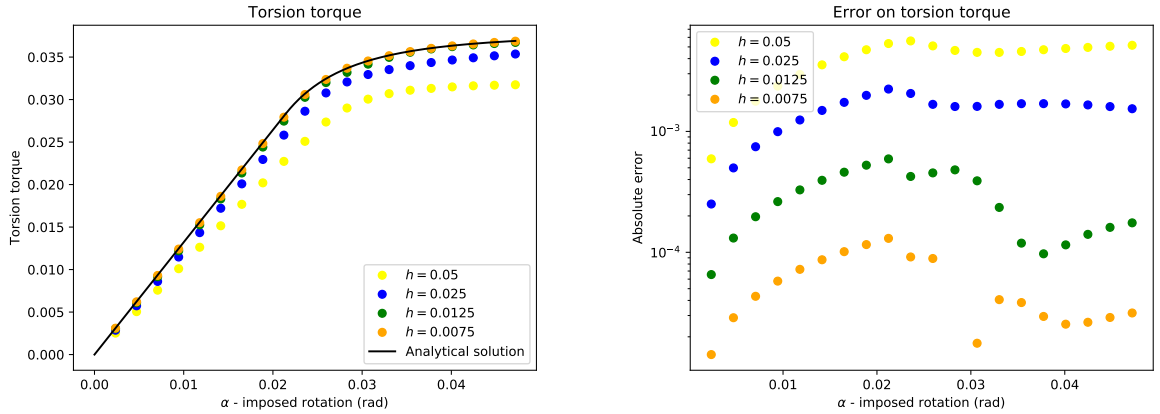

Figure 8: Beam in quasi-static torsion. Left: torque-angle response curve for the analytical solution and the DEM solution on various meshes. Right: difference between the analytical solution and the DEM solution on various meshes.

on a quarter of a planar section of the cylinder with a plane strain formulation. A sketch of the problem setup is presented in Figure 9. On the lateral sides of the quarter of cylinder, a null normal displacement and a null tangential component of the normal stress are enforced. The outer side of the cylinder is stress free ($\sigma \cdot n = 0$), and the inner pressure ϖ imposed on the inner side is linearly increased from 0 to $p_{\max} = \frac{2}{\sqrt{3}}\sigma_0 \ln\left(\frac{R_o}{R_i}\right)$, where $\sigma_0 = 250\text{N.m}^{-2}$ is the initial yield stress. The tangent plastic modulus is set to $E_t = \frac{1}{100}E$.

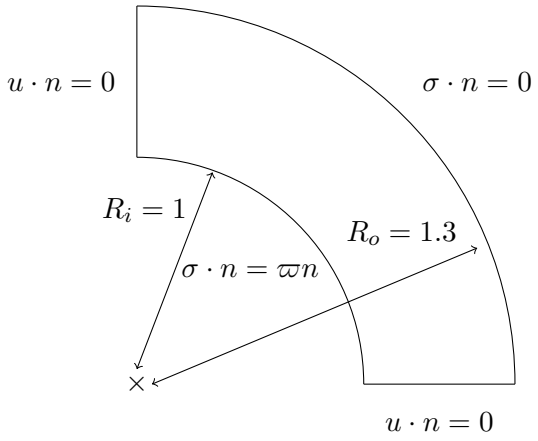

Figure 9: Inner swelling of an infinite cylinder: problem setup.

Table 6 reports the L^2-error on the displacement (evaluated as in Section 3.5) and on the cumulated plastic strain. The reference solution is computed on the finest mesh and is based on P^2-Lagrange FEM using the implementation available in [3]. The results in Table 6 show that the method converges at order 2 in the reconstructed displacement $\mathfrak{u}_h$ and at order 1 in the cumulated plastic strain p_h in the L^2-norm. The method also converges at order 1 in the energy norm (not reported for brevity).

h	dofs	$\|u - \mathfrak{u}_h\|_{L^2(\Omega)}$	order	$\|p - p_h\|_{L^2(\Omega)}$	order
0.07735	992	2.21e-4	-	2.20e-03	-
0.04217	3412	6.24e-5	2.05	1.13e-03	1.08
0.02879	7588	1.73e-5	2.50	6.47e-04	1.21
0.02172	13380	1.08e-5	2.32	4.88e-04	1.16
0.01464	29528	4.25e-6	2.33	2.96e-04	1.18

Table 6: Inner swelling of an infinite cylinder: size of the mesh, number of dofs, L^2-error in u and order of convergence, L^2-error in p and order of convergence.

5 Fully space-time discrete elasto-plasticity

In this section we consider the dynamic elasto-plasticity equations from Section 2. The time discretization is performed by means of an explicit, pseudo-energy conserving, time-integration scheme recently introduced in [18] and hereafter referred to as the MEMM scheme. The space discretization is achieved by means of the DEM scheme discussed in Section 3. Three-dimensional test cases are presented to assess the proposed methodology.

5.1 Time semi-discretization of dynamic elasto-plasticity

For simplicity we consider in this section only the time semi-discretization of the dynamic elasto-plasticity equations (9). We deal with the fully space-time discrete setting in the next section. The MEMM time-integration scheme is a two-step method of order two which ensures a discrete pseudo-energy conservation, if the integration of forces is exact, even for nonlinear systems. Symmetric Gaussian quadratures of the forces can be used in practice as long as they are of order at least two. The time interval $(0,T)$ is discretized using the time nodes $0 = t_0 < \ldots < t_n < \ldots < t_N = T$, and for simplicity we consider a constant time step Δt. We define the half-time nodes $t_{n+\frac{1}{2}} = \frac{1}{2}(t_n + t_{n+1})$ for all $n = 0, \ldots, N$. The time step is limited by a CFL condition which we specify in the fully discrete setting in the next section.

The key idea in the MEMM scheme is to approximate the displacement field at the time nodes by means of functions u^n, for all $n = 0, \ldots, N$, with u^0 specified by the initial condition on the displacement, and the velocity field at the half-time nodes by means of functions $v^{n+\frac{1}{2}}$, for all $n = 0, \ldots, N$, with $v^{\frac{1}{2}}$ specified by the initial condition on the velocity. For all $n = 0, \ldots, N$, given u^n and $v^{n+\frac{1}{2}}$, the MEMM scheme performs two substeps: (i) A time-dependent displacement field is predicted on the time interval $[t_n, t_{n+1}]$ using the free-flight expression $\tilde{u}(t) = u^n + (t - t_n)v^{n+\frac{1}{2}}$ for all $t \in [t_n, t_{n+1}]$; (ii) The velocity field $v^{n+\frac{3}{2}}$ is predicted by means of a quadrature on the time-integration of the forces in the time interval $[t_n, t_{n+1}]$. Let $\{t_{n,k}\}_{k\in\mathcal{K}}$ and $\{\omega_{n,k}\}_{k\in\mathcal{K}}$ be the nodes and the weights for the quadrature in the time interval $[t_n, t_{n+1}]$. We then set

$$\begin{cases} u^{n,k} = u^n + (t_{n,k} - t_n)v^{n+\frac{1}{2}}, & \forall k \in \mathcal{K}, \\ \dfrac{1}{2}m(v^{n+\frac{3}{2}} - v^{n-\frac{1}{2}}, \tilde{v}) = \displaystyle\sum_{k\in\mathcal{K}} \omega_{n,k}\Big(l(t_{n,k}, \tilde{v}) - a(\varepsilon_p^{n,k}; u^{n,k}, \tilde{v})\Big), & \forall \tilde{v} \in V_0, \\ (\varepsilon_p^{n,k}, p^{n,k}) = \texttt{PLAS\_EXP}(\varepsilon_p^{n,k-1}, p^{n,k-1}, \varepsilon^{n,k}), & \forall k \in \mathcal{K}, \end{cases} \tag{37}$$

where $\varepsilon^{n,k} := \varepsilon(u^{n,k})$ is known from the free-flight displacement prediction and where the state for the first Gauss node $k = 1$ comes from the previous time step or the initial condition. Given a triple $(\varepsilon_p^{\text{old}}, p^{\text{old}}, \varepsilon^{\text{new}})$, the procedure `PLAS_EXP` returns a pair $(\varepsilon_p^{\text{new}}, p^{\text{new}})$ such that, letting $\sigma^{\text{new}} := \mathbb{C} : (\varepsilon^{\text{new}} - \varepsilon_p^{\text{new}})$, we have

$$\begin{cases} \varphi(\sigma^{\text{new}}, p^{\text{new}}) \le 0, \\ \lambda^{\text{new}} := \delta p := p^{\text{new}} - p^{\text{old}} \ge 0, \quad \lambda^{\text{new}}\varphi(\sigma^{\text{new}}, p^{\text{new}}) = 0, \\ \delta\varepsilon_p := \varepsilon_p^{\text{new}} - \varepsilon_p^{\text{old}} = \lambda^{\text{new}} \dfrac{\partial\varphi}{\partial\sigma}(\mathbb{C} : (\varepsilon^{\text{new}} - \varepsilon_p^{\text{old}})). \end{cases} \tag{38}$$

The main difference with respect to the procedure `PLAS_IMP` described in (32) is on the increment of the tensor of remanent plastic strain.

5.2 Fully space-time discrete scheme

Full space-time discretization is achieved by combining the MEMM time-integration scheme described in the previous section with the DEM space discretization scheme from Section 3. For all $n = 1, \ldots, N$, we compute a discrete displacement field $u_h^n \in V_{hD}$ (recall that this space depends on n if the prescribed Dirichlet condition on the displacement is time-dependent) and a discrete velocity field $v_h^{n+\frac{1}{2}} \in W_{hD}$ where the Dirichlet condition on the velocity stems from the time-derivative of the prescribed displacement on the Dirichlet boundary $\partial\Omega_D$. Moreover, we compute a (tensor-free) tensor of remanent plastic strain $\varepsilon_{p,c}^{n,k}$ and a scalar cumulated plastic deformation $p_c^{n,k}$ for every mesh cell $c \in \mathcal{C}$ and every Gauss time-node $k \in \mathcal{K}$. We set $\varepsilon_{p,\mathcal{C}}^{n,k} :=$

$(\varepsilon_{p,c}^{n,k})_{c\in\mathcal{C}}$ and $p_{\mathcal{C}}^{n,k} := (p_c^{n,k})_{c\in\mathcal{C}}$. The fully discrete scheme reads as follows: For all $n = 1, \ldots, N$, given u_h^n, $v_h^{n-\frac{1}{2}}$ and $v_h^{n+\frac{1}{2}}$, compute $\{u_h^{n,k}\}_{k\in\mathcal{K}}$, $v_h^{n+\frac{3}{2}}$, $\{\varepsilon_{p,\mathcal{C}}^{n,k}\}_{k\in\mathcal{K}}$, and $\{p_{\mathcal{C}}\}_{k\in\mathcal{K}}$ such that

$$\begin{cases} u_h^{n,k} = u_h^n + (t_{n,k} - t_n) v_h^{n+\frac{1}{2}}, & \forall k \in \mathcal{K}, \\ \dfrac{1}{2} m_h(v_h^{n+\frac{3}{2}} - v_h^{n-\frac{1}{2}}, \tilde{v}_h) = \displaystyle\sum_{k\in\mathcal{K}} \omega_{n,k} \Big(l_h(t_{n,k}, \tilde{v}_h) - a_h(\varepsilon_{p,\mathcal{C}}^{n,k}; u_h^{n,k}, \tilde{v}_h) \Big), & \forall \tilde{v}_h \in V_{h0}, \\ (\varepsilon_{p,c}^{n,k}, p_c^{n,k}) = \texttt{PLAS\_EXP}(\varepsilon_{p,c}^{n,k-1}, p_c^{n,k-1}, \varepsilon_c^{n,k}), & \forall k \in \mathcal{K},\ \forall c \in \mathcal{C}, \end{cases} \tag{39}$$

where $\varepsilon_c^{n,k} := \varepsilon_c(\mathcal{R}(u_h^{n,k}))$. Moreover, m_h and l_h are, respectively, the discrete mass bilinear form and the discrete load linear form. For the first Gauss node $k = 1$, the first two arguments in `PLAS_EXP` come from the previous time step or the initial condition. The initial displacement u_h^0 and the initial velocity $v_h^{\frac{1}{2}}$ are evaluated by using the values of the prescribed initial displacement u_0 and the prescribed initial velocity v_0 at the cell barycenters and the boundary vertices.

The time step is restricted by the following CFL stability condition:

$$\Delta t < 2\sqrt{\frac{\mu_{\min}}{\lambda_{\max}}}, \tag{40}$$

where $\mu_{\min}$ is the smallest component of the diagonal mass matrix associated by the discrete mass bilinear form $m_h(\cdot,\cdot)$ and $\lambda_{\max}$ is the largest eigenvalue of the stiffness matrix associated the discrete stiffness bilinear form $a_h(0;\cdot,\cdot)$ (i.e., this maximal eigenvalue is computed in the worst-case scenario when there is no plasticity). The CFL condition (40) guarantees the stability of the MEMM time-integration scheme in the linear case [18], i.e., when there is no plasticity. We expect that this condition is still reasonable in the nonlinear case with plasticity since plasticity does not increase the stiffness of the material.

5.3 Numerical tests

This section contains two three-dimensional test cases: a beam in dynamic flexion and a beam in dynamic torsion. We use the midpoint quadrature for the integration of the forces in each time step within the MEMM time-integration scheme. We refer the reader to [18] for a study of the influence of the quadrature on the scheme accuraccy for various nonlinear problems with Hamiltonian dynamics.

5.3.1 Beam in dynamic flexion

This test case consists in computing the oscillations of an elastic and linearly isotropic plastic beam of length $L = 1\text{m}$ with a rectangular section of $0.04 \times 0.1\text{m}^2$. The simulation time is $T = 2.5\text{s}$. The beam is clamped at one end, it is loaded by a uniform vertical traction $g(t)$ at the other end, and the four remaining lateral faces are stress free ($\sigma \cdot n = 0$). The load term $g(t)$ is defined as

$$g(t) := \begin{cases} -e_x & \text{for } 0 \le t \le \frac{1}{5}T, \\ 0 & \text{for } \frac{1}{5}T \le t \le T. \end{cases} \tag{41}$$

Figure 10 displays the problem setup. The material parameters are $E = 1\text{MPa}$ for the Young modulus, $\nu = 0.3$ for the Poisson ratio, $\rho = 1\text{kg}\cdot\text{m}^{-3}$ for the density, $\sigma_0 = 25\text{Pa}$ for the yield stress, and $E_t = \frac{1}{100}E$ for the tangent plastic modulus. The present three-dimensional implementation used as a starting point [3], where FEM and an implicit time-integration scheme are considered for a purely elastic material.

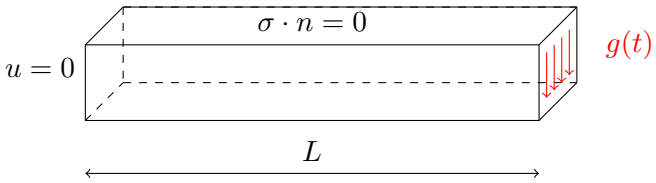

Figure 10: Beam in dynamic flexion: problem setup.

The proposed DEM is compared to P^1-Lagrange FEM. A first computation is performed with two coarse meshes, one for the DEM leading to 1281 vector-valued dofs and one for the P^1-Lagrange FEM leading to 1266 vector-valued dofs. The time step is $\Delta t_{\text{coarse}} = 2.6{\cdot}10^{-6}$, which is stable for the explicit integration for both methods. A second computation is performed on two finer meshes, leading to 13446 dofs for the DEM and to 14004 dofs for the P^1-Lagrange FEM. The stable time-step for both methods is $\Delta t_{\text{fine}} = 6.2{\cdot}10^{-7}$. As already mentioned, the MEMM time-integrator hinged on a midpoint quadrature. Higher-order symmetric quadratures have been found to give overlapping results with respect to the midpoint quadrature. In all the computations, the time-discretization error is negligeable with respect to the space-discretization error.

The displacement and velocity at the center of the loaded tip of the beam are compared in Figure 11 for the coarse and the fine meshes. We notice the discrepancy between DEM and FEM predictions on the coarse meshes and that this discrepancy decreases significantly on the fine meshes. (The FEM simulation on the fine mesh has not yet been fully completed at the time of submission, but the reported results already show the main behavior.)

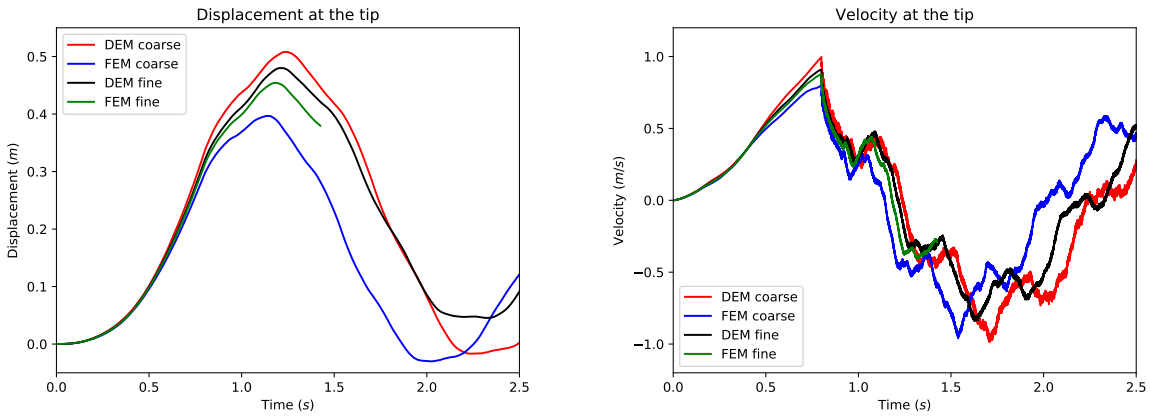

Figure 11: Beam in dynamic flexion: comparison between the proposed scheme (DEM) and a finite element solution (FEM) on coarse and fine meshes. Left: Displacement at the loaded tip of the beam. Right: Velocity at the same point.

Figure 12 shows the balance of energies. One can first notice that the total energy for both DEM and FEM space semi-discretizations is well preserved by the MEMM time-integrator since the total mechanical energy (kinetic energy, elastic energy and plastic dissipation) and the work of the external load are perfectly balanced at all times. We also notice that the amount of plastic dissipation is rather significant at the end of the simulation.

Figure 13 presents some further results of the DEM computations on the fine mesh so as to visualize at three different times during the simulation the spatial localization of the von Mises equivalent stress, the cumulated plastic strain, and the trace of the stress tensor. One

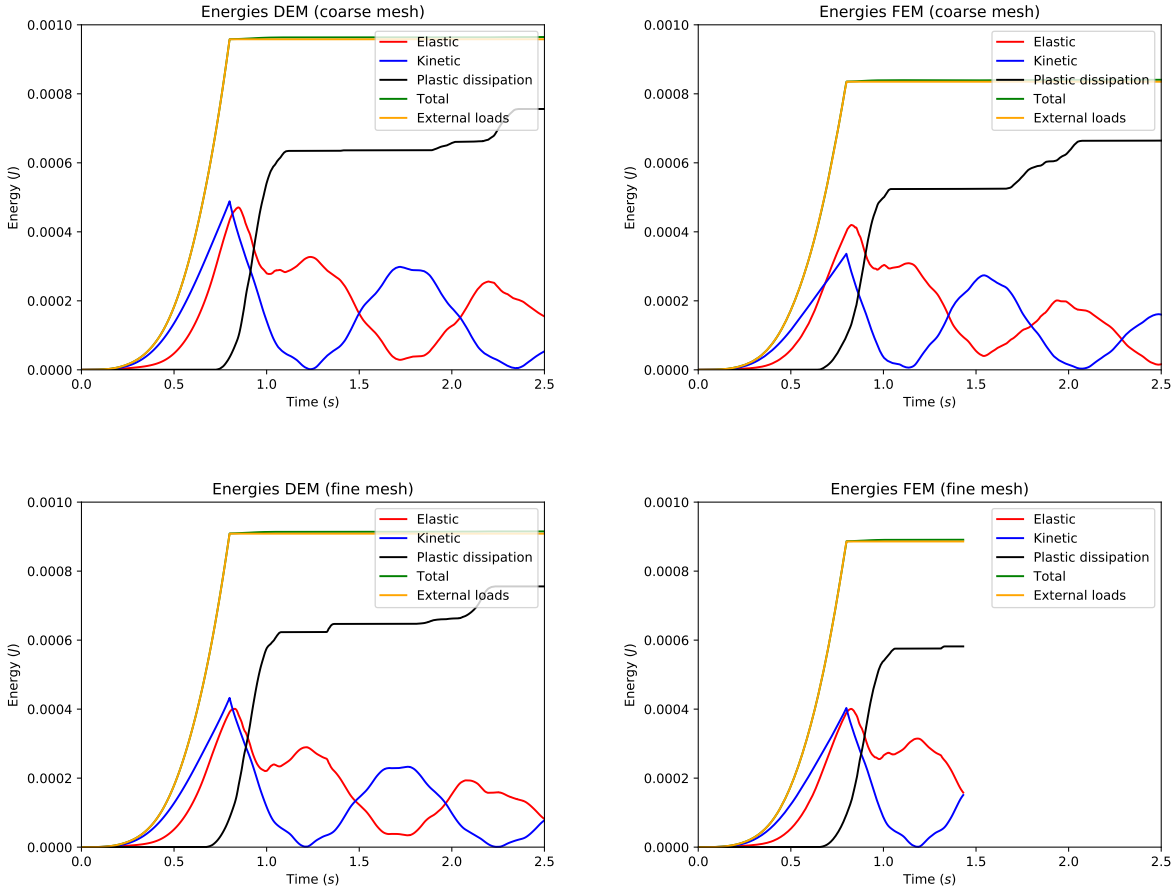

Figure 12: Beam in dynamic flexion: energies during the simulation. Above: coarse mesh. Below: fine mesh. Left: DEM. Right: FEM.

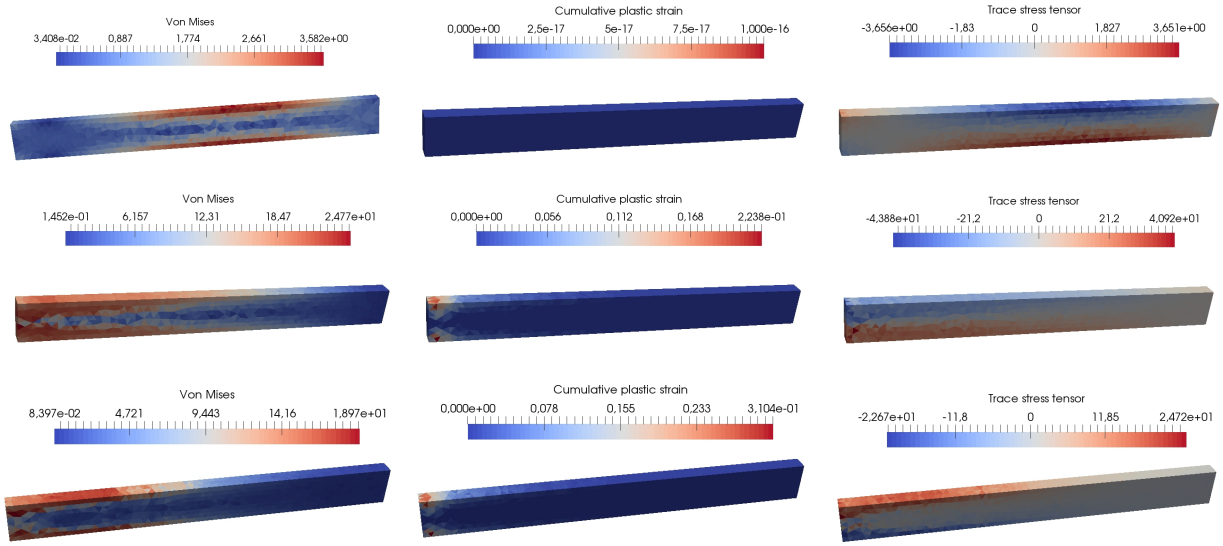

Figure 13: Beam in dynamic flexion: DEM on the fine mesh. Von Mises equivalent stress (left column), p (middle column) and $\mathrm{tr}(\sigma)$ (right column) at $t = \frac{1}{10}T$ (top line), $t = \frac{1}{2}T$ (middle line) and $t = T$ (bottom line).

can see that the plastic strain is concentrated close to the clamped tip of the beam, where the material undergoes the greatest stresses. The method does not exhibit any locking due to plastic incompressibility as indicated by the smooth behavior of the trace of the stress tensor.

5.3.2 Beam in dynamic torsion

The setting is similar to the quasi-static torsion test case presented in Section 4.3.2. The two differences are the plastic law which is no longer perfect but linearly hardening as in Section 5.3.1, and the boundary conditions on one side of the beam. Figure 14 shows the problem setup. On one of its extremities the beam is clamped, and on the other extremity the following normal stress is imposed:

$$g(t) = \mu\alpha(t)\frac{r}{L}e_\theta, \tag{42}$$

where r and e_θ are defined in Section 4.3.2. The angle $\alpha(t)$ is increased from 0 at $t = 0$ to $5\alpha_y$ at $t = T = 0.5$s, where α_y is the yield angle defined in Section 4.3.2. The plastic parameters are the same as those in Section 5.3.1.

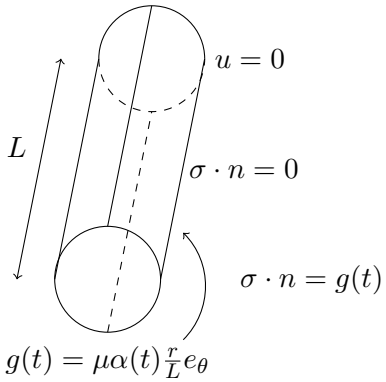

Figure 14: Beam in dynamic torsion: problem setup.

The coarse meshes lead to 2008 vector-valued displacement dofs for the DEM and to 2170 vector-valued displacement dofs for the P^1-Lagrange FEM. The time step is $\Delta t_{\text{coarse}} = 1.8{\cdot}10^{-6}$s, which is stable for both computations. The fine meshes lead to 6978 vector-valued dofs for the DEM and to 6584 vector-valued dofs for the P^1-Lagrange FEM. The time step is $\Delta t_{\text{fine}} = 1.9 \cdot 10^{-6}$s, which is also stable for both computations. Though surprising at first glance, the identity $\Delta t_{fine} > \Delta t_{coarse}$ can be seen as a byproduct of the facet reconstruction algorithm presented in Section 3.3. Indeed the interpolation procedure seems to rely on more regular neighboring simplices in the case of the fine mesh. The MEMM time-integration scheme with a midpoint quadrature is used. In all computations, the time-discretization error is negligeable with respect to the space-discretization error.

The comparison between the two methods is performed by considering the displacement and the velocity of the point of coordinates $(0.9R, 0, \frac{1}{6}L)$ and over the simulation time T. The results are reported in Figure 15. (The FEM simulation on the fine mesh has not yet been fully completed at the time of submission, but the reported results already show the main behavior.) We notice that the value for the simulation time is too long for the simulation to remain physically relevant within the small strain assumption owing to the large value reached by the angular displacement of the reference point. However this setting allows us to reach substantial amounts of plastic dissipation and thereby to probe the robustness of the space semi-discretization methods with respect to incompressibility. Recall that the remanent plastic

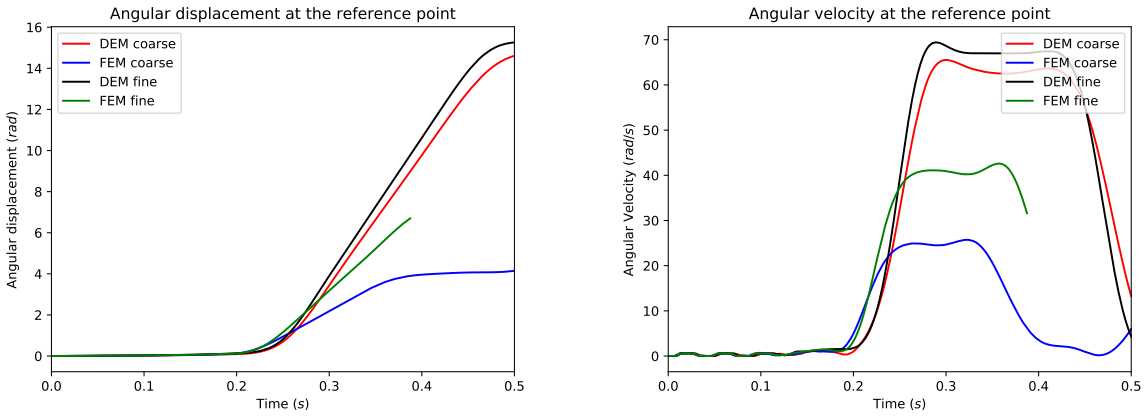

Figure 15: Beam in dynamic torsion: comparison between DEM and FEM. Left: Displacement at the chosen point. Right: Velocity at the same point.

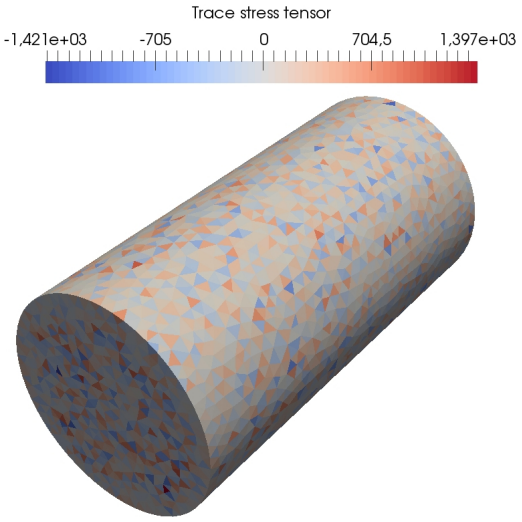

Figure 16: Beam in dynamic torsion: FEM (fine mesh). $\mathrm{tr}(\sigma)$ at $t = \frac{1}{2}T$.

strain tensor is trace-free, so that the stress tensor is nearly deviatoric in the entire beam at the end of the simulation. Such a situation is challenging for the P^1-Lagrange FEM since this method is known to lock in the incompressible limit. This explains the strong discrepancy between FEM and DEM in Figure 15. To highlight the volumetric locking incurred by FEM, Figure 16 displays at the time $t = \frac{1}{2}T$ the trace of the stress tensor predicted by FEM. Significant oscillations are visible in the whole beam (the amplitude of these oscillations is about ten times the maximal value of the von Mises equivalent stress). Figure 17 reports the energies on the coarse and the fine meshes for DEM and FEM. As in Figure 15, significant discrepancies between DEM and FEM are again observed. Moreover we notice as in the previous test case the prefect balance of the work of external loads with the different components of the mechanical energy. Finally we observe that the fraction of elastic energy is larger for FEM than for DEM, whereas FEM underestimates the plastic strain.

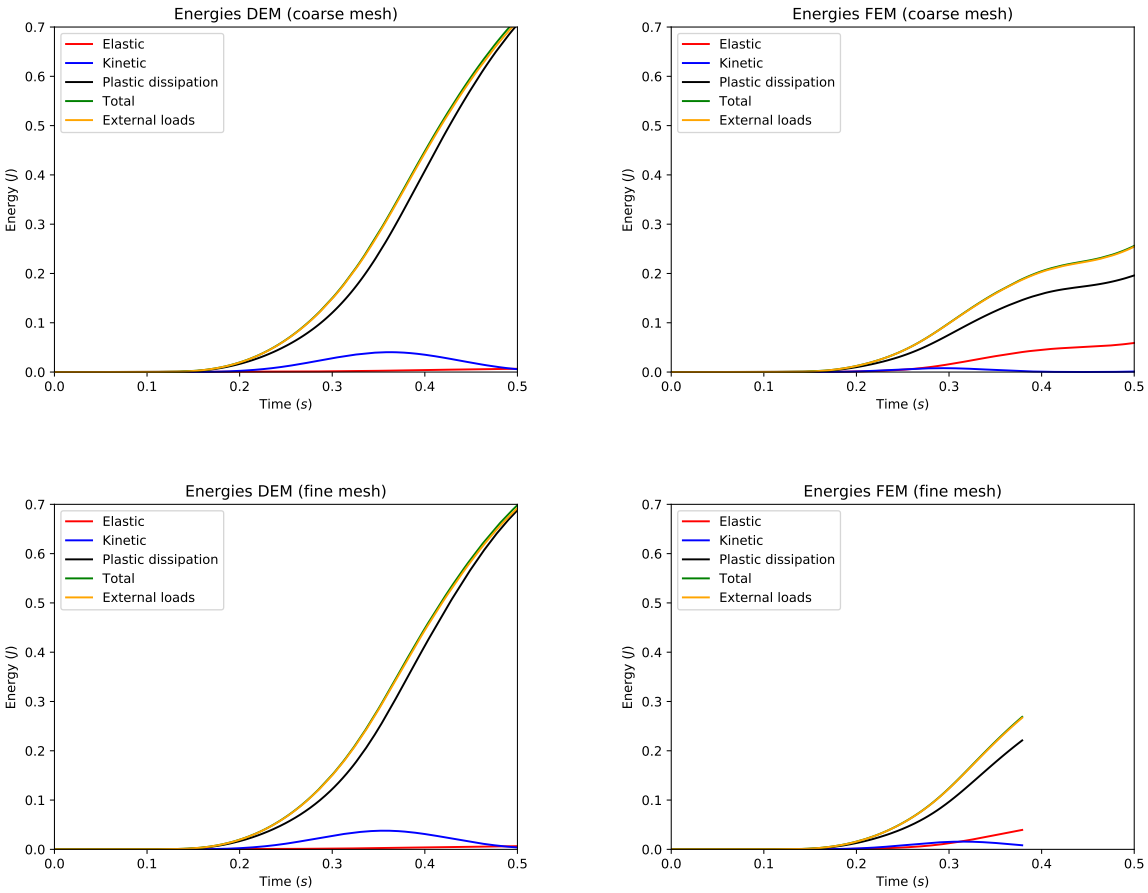

Figure 17: Beam in dynamic torsion: energies during the simulation. Above: coarse mesh. Below: fine mesh. Left: DEM. Right: FEM.

Figure 18 presents some further results of the DEM computations on the fine mesh so as to visualize at three different times during the simulation the spatial localization of the von Mises equivalent stress, the cumulated plastic strain, and the trace of the stress tensor. The magnitude of the oscillations of the trace of the stress tensor is significantly smaller than the magnitude of the von Mises equivalent stress.

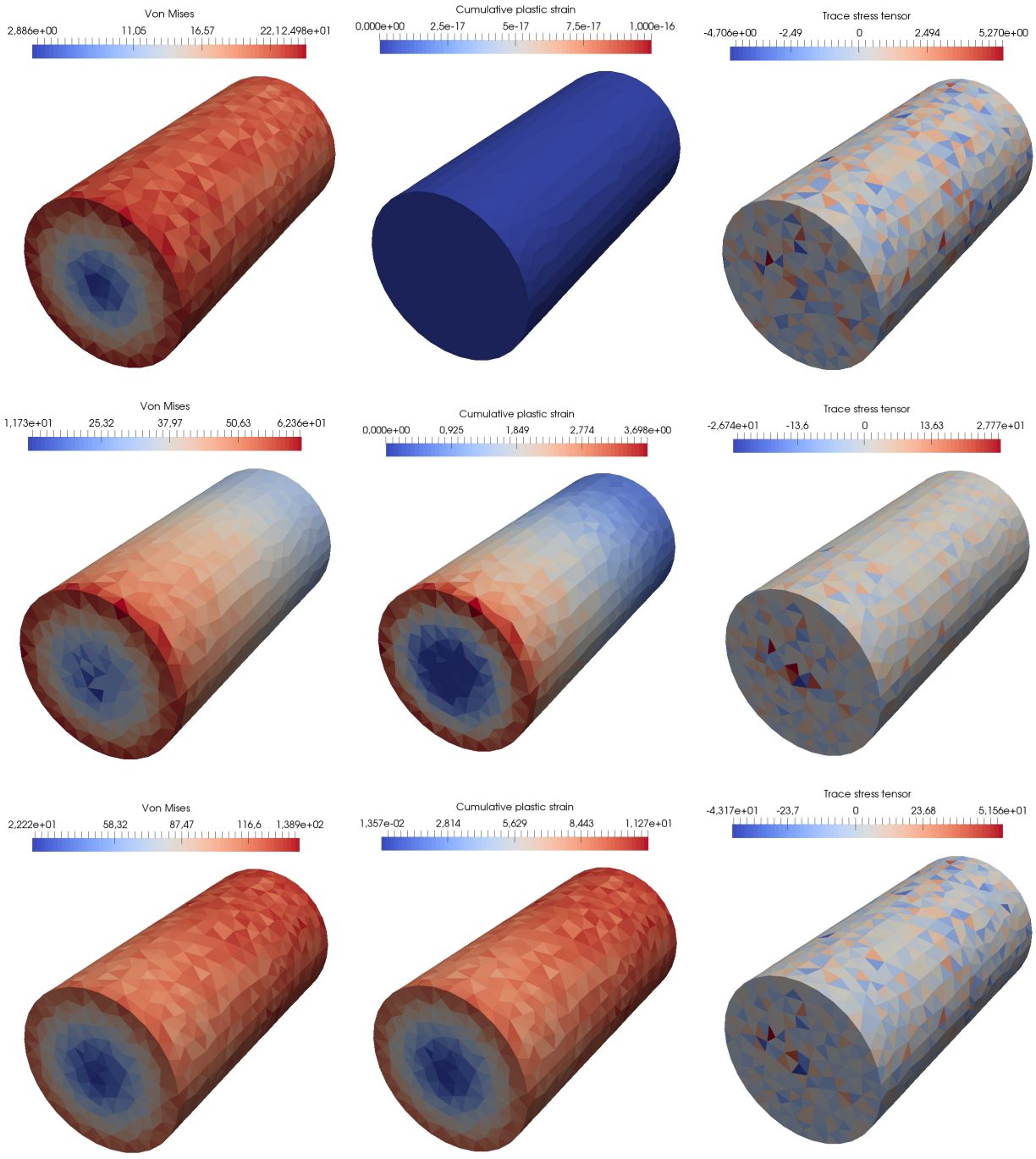

Figure 18: Beam in dynamic torsion: DEM on the fine mesh. Von Mises equivalent stress (left column), p (middle column) and $\mathrm{tr}(\sigma)$ (right column) at $t = \frac{1}{10}T$ (top line), $t = \frac{1}{2}T$ (middle line) and $t = T$ (bottom line).

6 Conclusion

We have presented a new Discrete Element Method which is a consistent discretization of a Cauchy continuum and which only requires continuum macroscopic parameters as the Young modulus and the Poisson ratio for its implementation. The displacement degrees of freedom are attached to the barycenters of the mesh cells and to the boundary vertices. The key idea is to reconstruct displacements on the mesh facets and then to use a discrete Stokes formula to devise a piecewise constant gradient and linearized strain reconstructions. A simple geometric pre-processing has been devised to ensure that for almost all the mesh facets, the reconstruction is based on an interpolation (rather than extrapolation) formula and we have shown by numerical experiments that this choice can produce highly beneficial effects in terms of the largest eigenvalue of the stiffness matrix, and thus on the time step restriction within explicit time-marching schemes. Moreover, in the case of elasto-plastic behavior, the internal variables for plasticity are piecewise-constant in the mesh cells. The scheme has been tested on quasi-static and dynamic test cases using a second-order, explicit, energy-conserving time-marching scheme. Future work can include adapting the present framework to dynamic cracking and fragmentation as well as to Cosserat continua.

Acknowledgements

The authors would like to thank K. Sab (Navier, ENPC) and L. Aubry (CEA) for fruitful discussions. The authors would also like to thank J. Bleyer (Navier, ENPC) for his help in dealing with the Fenics implementations. The PhD fellowship of the first author was supported by CEA.

References

[1] D. André, J. Girardot, and C. Hubert. A novel dem approach for modeling brittle elastic media based on distinct lattice spring model. *Computer Methods in Applied Mechanics and Engineering*, 350:100–122, 2019.

[2] D. André, M. J., I. Iordanoff, J.-L. Charles, and J. Néauport. Using the discrete element method to simulate brittle fracture in the indentation of a silica glass with a blunt indenter. *Computer Methods in Applied Mechanics and Engineering*, 265:136–147, 2013.

[3] J. Bleyer. Numerical tours of computational mechanics with FEniCS, 2018. `https://zenodo.org/record/1287832#.Xbsqdvco85k`.

[4] M. Budninskiy, B. Liu, Y. Tong, and M. Desbrun. Power coordinates: a geometric construction of barycentric coordinates on convex polytopes. *ACM Transactions on Graphics (TOG)*, 35(6):241, 2016.

[5] C. Carstensen. Numerical analysis of the primal problem of elastoplasticity with hardening. *Numerische Mathematik*, 82(4):577–597, 1999.

[6] M. A. Celigueta, S. Latorre, F. Arrufat, and E. Oñate. Accurate modelling of the elastic behavior of a continuum with the discrete element method. *Comput. Mech.*, 60(6):997–1010, 2017.

[7] Z. Chen and H. Chen. Pointwise error estimates of discontinuous galerkin methods with penalty for second-order elliptic problems. *SIAM Journal on Numerical Analysis*, 42(3):1146–1166, 2004.

[8] P. Cundall and O. Strack. A discrete numerical model for granular assemblies. *geotechnique*, 29(1):47–65, 1979.

[9] D. A. Di Pietro. Cell centered Galerkin methods for diffusive problems. *ESAIM: Mathematical Modelling and Numerical Analysis*, 46(1):111–144, 2012.

[10] J. Droniou, R. Eymard, T. Gallouët, C. Guichard, and R. Herbin. *The gradient discretisation method*, volume 82. Springer, 2018.

[11] R. Eymard, T. Gallouët, and R. Herbin. A finite volume scheme for anisotropic diffusion problems. *Comptes Rendus Mathématique*, 339(4):299–302, 2004.

[12] R. Eymard, T. Gallouët, and R. Herbin. Discretization of heterogeneous and anisotropic diffusion problems on general nonconforming meshes sushi: a scheme using stabilization and hybrid interfaces. *IMA Journal of Numerical Analysis*, 30(4):1009–1043, 2009.

[13] W. Han and X. Meng. Error analysis of the reproducing kernel particle method. *Comput. Methods Appl. Mech. Engrg.*, 190(46-47):6157–6181, 2001.

[14] W. Han and B. D. Reddy. *Plasticity: mathematical theory and numerical analysis*, volume 9. Springer Science & Business Media, 2012.

[15] W.G. Hoover, W.T. Ashurst, and R.J. Olness. Two-dimensional computer studies of crystal stability and fluid viscosity. *The Journal of Chemical Physics*, 60(10):4043–4047, 1974.

[16] M. Jebahi, D. André, I. Terreros, and I. Iordanoff. *Discrete element method to model 3D continuous materials*. John Wiley & Sons, 2015.

[17] C. Labra and E. Oñate. High-density sphere packing for discrete element method simulations. *Comm. Numer. Methods Engrg.*, 25(7):837–849, 2009.

[18] F. Marazzato, A. Ern, C. Mariotti, and L. Monasse. An explicit pseudo-energy conserving time-integration scheme for hamiltonian dynamics. *Computer Methods in Applied Mechanics and Engineering*, 347:906 – 927, 2019.

[19] L. Monasse and C. Mariotti. An energy-preserving discrete element method for elastodynamics. *ESAIM: Mathematical Modelling and Numerical Analysis*, 46:1527–1553, 2012.

[20] H. Nilsen, I. Larsen, and X. Raynaud. Combining the modified discrete element method with the virtual element method for fracturing of porous media. *Comput. Geosci.*, 21(5-6):1059–1073, 2017.

[21] J. C. Simo and R. L. Taylor. Consistent tangent operators for rate-independent elastoplasticity. *Computer methods in applied mechanics and engineering*, 48(1):101–118, 1985.

[22] N. Q. Son. On the elastic plastic initial-boundary value problem and its numerical integration. *International Journal for Numerical Methods in Engineering*, 11(5):817–832, 1977.

[23] M. Spellings, R. L. Marson, J. A. Anderson, and S. C. Glotzer. GPU accelerated discrete element method (DEM) molecular dynamics for conservative, faceted particle simulations. *J. Comput. Phys.*, 334:460–467, 2017.